



<b>Title</b>	Analysis of the tropical tropopause layer using the Nonhydrostatic Icosahedral Atmospheric Model (NICAM): Aqua planet experiments
<b>Author(s)</b>	Kubokawa, H.; Fujiwara, M.; Nasuno, T.; Satoh, M.
<b>Citation</b>	Journal of Geophysical Research, 115(D8), D08102 <a href="https://doi.org/10.1029/2009JD012686">https://doi.org/10.1029/2009JD012686</a>
<b>Issue Date</b>	2010-04-27
<b>Doc URL</b>	<a href="http://hdl.handle.net/2115/64813">http://hdl.handle.net/2115/64813</a>
<b>Rights</b>	Copyright 2010 American Geophysical Union.
<b>Type</b>	article
<b>File Information</b>	Kubokawa_et_al-2010-Journal_of_Geophysical_Research__Atmospheres_(1984-2012).pdf



[Instructions for use](#)



## Analysis of the tropical tropopause layer using the Nonhydrostatic Icosahedral Atmospheric Model (NICAM): Aqua planet experiments

H. Kubokawa,<sup>1</sup> M. Fujiwara,<sup>1</sup> T. Nasuno,<sup>2</sup> and M. Satoh<sup>2,3</sup>

Received 17 June 2009; revised 13 October 2009; accepted 12 November 2009; published 22 April 2010.

[1] The dynamical characteristics of the tropical tropopause layer (TTL) are investigated using the Nonhydrostatic Icosahedral Atmospheric Model (NICAM) run on the Earth Simulator under an aqua planet condition. Two experiments are performed: one with a 3.5 km horizontal spacing and a three-dimensional snapshot output and another with a 7 km horizontal spacing and 3-hourly averages for 1 month. The number of vertical levels is 54 and the model top is at 40 km; the vertical spacing in and around the TTL is  $\sim 700$  m. Large-scale organized convection associated with convectively coupled equatorial Kelvin waves prevails around the equator. The zonal mean vertical distribution of cloud top height near the equator shows a realistic trimodal structure. The simulation results reveal that cumulus clouds penetrate the lapse-rate tropopause and the bottom boundary of the TTL (defined as the lapse rate minimum) for  $\sim 0.1\%$  and  $\sim 25\%$ , respectively, in the equatorial area. The frequency distribution of vertical wind may provide a good indicator of the TTL bottom boundary. A significant reduction in the speed of strong vertical winds is observed at  $\sim 16$  km. High variability in temperature and the water vapor mixing ratio observed around the tropopause is mainly caused by equatorial Kelvin waves generated by the organized convection in these experiments. Horizontal variability in tropopause height over a large-scale convective system is much smaller than that in the area of Kelvin waves. The gravity waves generated by this large-scale convective system locally control the temperature around the tropopause. In addition, large-amplitude gravity waves with a scale of 600 km are superimposed on the cold phase of Kelvin waves, producing one of the coldest regions around the tropopause. It is suggested that the combination of Kelvin waves and gravity waves may be one of the most effective dehydration processes in the TTL.

**Citation:** Kubokawa, H., M. Fujiwara, T. Nasuno, and M. Satoh (2010), Analysis of the tropical tropopause layer using the Nonhydrostatic Icosahedral Atmospheric Model (NICAM): Aqua planet experiments, *J. Geophys. Res.*, *115*, D08102, doi:10.1029/2009JD012686.

### 1. Introduction

[2] The tropical tropopause is the main entranceway for dehydrated tropospheric air into the stratosphere [e.g., Brewer, 1949; Holton *et al.*, 1995]. Highwood and Hoskins [1998] and Folkins *et al.* [1999] suggested the existence of a transition layer around the tropical tropopause; this layer is now termed the tropical tropopause layer (TTL) (see also the review by Fueglistaler *et al.* [2009]). Air in the TTL has the characteristics of both the troposphere and stratosphere,

although the direct influence of deep convection is considered to be small. The TTL is defined as the layer between the level of maximum convective outflow, which is often defined in terms of the minimum temperature lapse rate [Gettelman and Birner, 2007], and the cold point tropopause.

[3] Holton and Gettelman [2001] suggested that horizontal processing of air by passage through the Western Pacific cold trap is an effective means to explain the extreme aridity of the equatorial stratosphere. This idea was further investigated by Fueglistaler *et al.* [2005] based on a comparison of reanalysis data with satellite measurements of stratospheric water vapor. The results of these trajectory studies suggest that the quasi-horizontal transport process is indeed essential for dehydration of the stratosphere and that subgrid-scale processes such as cumulus convection are possibly of secondary importance. The role of deep cumulus convection in dehydration was discussed extensively during

<sup>1</sup>Graduate School of Environmental Science, Hokkaido University, Sapporo, Japan.

<sup>2</sup>Research Institute for Global Change, Japan Agency for Marine-Earth Science and Technology, Yokohama, Japan.

<sup>3</sup>Center for Climate System Research, University of Tokyo, Kashiwa, Japan.

the 1980s and has recently reemerged as a research focus. The above trajectory studies are difficult, in principle, to address the importance of convection. In the following paragraphs, we present a brief review of studies that examined the role of deep convection in stratospheric dehydration.

[4] *Johnston and Solomon* [1979] proposed that intense thunderstorms that partly penetrate the tropopause may either hydrate the stratosphere via ice crystal transport or dehydrate the stratosphere via the adiabatic cooling of penetrating air. The authors also noted that thunderstorms are the only possible sink for stratospheric water. *Danielsen* [1982] proposed an effective dehydration mechanism associated with radiatively destabilized, thick anvil cirrus that may remain around the tropopause for 5–10 h. *Danielsen* [1993] made aircraft measurements in the “stratospheric fountain” region [*Newell and Gould-Stewart*, 1981] (i.e., tropical western Pacific during the northern winter), where and when the tropopause is coldest, and found a case in which the altitude of the minimum water vapor mixing ratio corresponds to the level of minimum temperature.

[5] Tropical convection generates various modes of atmospheric waves that propagate upward into the stratosphere. The role of such waves in dehydration around the tropical tropopause region was first recognized during the 1990s. *Pfister et al.* [1993] demonstrated the role of gravity waves generated by a tropical cyclone in controlling variations in tropopause temperature, during the same campaign as that of *Danielsen* [1993]. *Tsuda et al.* [1994] found that equatorial Kelvin waves strongly modify the tropopause temperature distribution, and discussed the possible role of such waves in stratosphere-troposphere exchange. The role of Kelvin waves in the transport of stratospheric, dry, ozone-rich air from the stratosphere to troposphere has been discussed previously based on balloon-borne measurements [*Fujiwara et al.*, 1998, 2001], the results of a general circulation model [*Fujiwara and Takahashi*, 2001]. *Fujiwara and Takahashi* [2001] suggested that Kelvin waves around the tropopause are excited by organized tropical convection, meaning that equatorial waves and organized clouds are both essential and constitute a large-scale system that controls transport and dehydration around the tropical tropopause.

[6] The TTL concept, which emerged in the late 1990s, indicates the essential role of horizontal transport and large-scale waves (rather than penetrating cumulonimbus clouds) in dehydration. However, *Sherwood and Dessler* [2000, 2001] proposed that the TTL should be viewed as an analogue of the entrainment zone around the top of the planetary boundary layer, and that deep convection which penetrates the TTL is the primary control on dehydration in this layer, and hence the main control on concentrations of water vapor in the stratosphere.

[7] Recent studies, based on analyses of satellite data, have estimated the frequency of deep convective clouds reaching the TTL and lower stratosphere. *Gettelman et al.* [2002] investigated brightness temperature data from geostationary satellites and found that 0.25%–0.75% of tropical clouds overshoot the tropopause. It should be noted that *Sherwood et al.* [2004] indicated that the cloud top altitudes estimated from geostationary satellite data are ~1 km lower than those estimated from ground-based radar data. There-

fore, the results of *Gettelman et al.* [2002] may represent the lower limit of cloud top height. Using Tropical Rainfall Measurement Mission (TRMM) satellite-borne radar data, *Liu and Zipser* [2005] showed that the cloud top altitude over the continents is higher than that over the ocean, and that 1.3% and 0.1% of tropical convection systems reach 14 km and the 380 K potential temperature level, respectively. *Dessler et al.* [2006] analyzed cloud-top height data obtained from Geoscience Laser Altimeter System (GLAS), carried onboard the Ice, Cloud, and Land Elevation Satellite (ICESat) and found that 0.34% of tropical clouds overshoot the tropopause.

[8] Mesoscale models and cloud-resolving models may be suitable for examining the role of deep convection in controlling dehydration within the TTL and in the formation of the TTL itself. *Potter and Holton* [1995] were the first to use a mesoscale model to investigate this problem, and they emphasized the role of convectively generated gravity waves rather than penetrating clouds. *Kuang and Bretherton* [2004] investigated the heat balance of the TTL using a model that explicitly calculates vertical winds without a cumulus parameterization for idealized cases, and found that deep convection acts to cool the TTL via turbulent heat-flux divergence. *Küpper et al.* [2004] used a mesoscale three-dimensional cloud-resolving model and discussed the relative contributions of cumulus clouds and slow, large-scale nonconvective ascent to the transport of mass and moisture into the stratosphere. The authors showed that nonconvective mass flux into the stratosphere is 2 orders of magnitude greater than cumulus mass flux, and that gravity waves contribute to cooling around the tropopause. *Chaboureau et al.* [2007] simulated a tropical convection case over Brazil (22°S) in February 2005, when high-altitude aircraft measurements were conducted around the tropopause [*Corti et al.*, 2008]. Both the simulation results and aircraft measurements indicated hydration (rather than dehydration) of the lower stratosphere due to ice crystals lofted by cumulonimbus clouds.

[9] Mesoscale models and cloud-resolving models are usually restricted to limited horizontal domains because of their huge computational cost. The results derived from such models may be strongly dependent on the applied boundary conditions, and such models inherently lack interaction between small-scale to mesoscale disturbances and large-scale disturbances to the general circulation. In the tropics, however, it is well known that such interaction is essential [e.g., *Madden and Julian*, 1994].

[10] Here, we address this problem using a global nonhydrostatic model: the Nonhydrostatic Icosahedral Atmospheric Model (NICAM) [*Tomita and Satoh*, 2004; *Satoh et al.*, 2008]. NICAM was developed at the Japan Agency for Marine-Earth Science and Technology (JAMSTEC) and the Center for Climate System Research (CCSR), University of Tokyo, with the aim of enabling global cloud-resolving modeling with a horizontal resolution down to the order of 1–10 km, making use of massive parallel computers such as the Earth Simulator. In this paper, we analyze data from the first set of full NICAM experiments under an aqua planet condition. Using this data set, *Tomita et al.* [2005] showed the existence of realistic features of the tropical atmosphere, including hierarchical cloud structures, intraseasonal oscillations similar to Madden-Julian Oscillation [*Madden and*

Julian, 1994], and diurnal cycles in precipitation. *Nasuno et al.* [2007, 2008] further investigated the tropical organized clouds in the data set and concluded that the intraseasonal oscillations are associated with convectively coupled equatorial waves. *Nasuno* [2008] used the same data set to investigate equatorial zonal mean zonal winds indicative of superrotation at the equator, and found that these winds are mainly controlled by the momentum transport associated with planetary-scale disturbances, particularly the moist Kelvin wave modes.

[11] In the present paper, we use NICAM aqua planet data to investigate the TTL in term of cloud top height statistics (section 4.1), major disturbances that control temperature (section 4.2), and the water vapor variations (section 4.3). The remainder of this paper is organized as follows. Section 2 provides details of NICAM and the aqua planet experiments, section 3 presents the general characteristics of the model atmosphere obtained from the experiments, section 4 provides the results and discusses their implications for the TTL, and finally, section 5 lists the conclusions.

## 2. Model Descriptions

[12] The dynamical core of NICAM is based on a non-hydrostatic scheme, without cumulus parameterizations [Tomita and Satoh, 2004; Satoh et al., 2008]. The horizontal grid is a modified icosahedral grid, and the cloud microphysical scheme proposed by Grabowski [1998] is applied. Two prognostic variables, precipitating and airborne hydrometeors, are defined, and liquid and ice phases are diagnosed by the temperature-dependent fractional ratio; there are four hydrometeors: cloud water, cloud ice, rain, and snow. The radiation scheme is based on that proposed by Nakajima et al. [2000], and the level-2 closure scheme by Mellor and Yamada [1974] is used for diffusion processes. Surface flux is approximated by the bulk method proposed by Louis [1979].

[13] In this experiment, the Earth is fully covered by ocean with zonally uniform sea surface temperature (SST) that is highest at the equator (27°C) and decreases with increasing latitude, following the standard SST profile (STD) of Neale and Hoskins [2000]. A persistent equinox is assumed during the entire integration period, whereby the Sun is always moving over the equator. The number of vertical levels is 54, with the model top at ~40 km, resulting in ~700 m spacing between levels in and around the TTL. The horizontal spacing of the icosahedral grid system is 14 km for the first run, 7 km for the second run, and 3.5 km for the final run. The initial condition was prepared with a 3.5 year integration of a T42-59-vertical-level atmospheric general circulation model (AGCM) (CCSR/National Institute for Environmental Studies/FRCGC AGCM version 5.7 [Numaguti et al., 1997]). The zonal mean climatology obtained from the last 3 years of AGCM integration was interpolated onto the 14 km grid of the NICAM, and the 14 km grid version of the NICAM was integrated for 90 days. Next, the data on the 60th day of the 14 km grid run was interpolated onto the 7 km grid, and the 7 km grid version of the NICAM was integrated for 40 days. Finally, the data on the 20th day of the 7 km run was interpolated onto the 3.5 km grid version, which was then integrated for 10 days. The full three-dimensional outputs are only available as 3 h averages

outputted every 3 h from the 0th day to the 30th day for the 7 km grid run, and for a snapshot on the 5th day for the 3.5 km grid run, which corresponds to the 25th day of the 7 km grid run. These two data sets are analyzed in the present paper. It should be noted that the three-dimensional 7 km grid outputs were averaged onto the 14 km grids to reduce the amount of data. Output parameters are three-dimensional winds, thermodynamic parameters, water vapor, and four condensation variables. There are no outputs of radiative and diffusion parameters.

## 3. General Characteristics of the Aqua Planet Experiment

[14] Figure 1 shows the zonal mean fields of zonal wind, temperature, and meridional and vertical winds using 3.5 km grid snapshot data. The results from the 7 km grid calculations are generally similar to those obtained from 3.5 km grid data. Figure 1a shows that the tropical troposphere above 5 km is westerly on average and that subtropical westerly jets occur at around 13 km. The zonal mean equatorial westerlies are also observed in the upper troposphere above 12 km in the 7 km grid data. *Nasuno* [2008] proposed that this equatorial westerly (i.e., a superrotation) is mainly influenced by the effects of Kelvin wave modes. The 5°S–5°N mean temperature and height of the cold-point tropopause (CPT) are on average 181.1 K and 18.2 km, respectively; these values are colder and higher, respectively, than the observed zonal mean tropical CPT in March (191 K, 17.1 km) [Seidel et al., 2001]. This is mainly caused by a too low initial condition. The 4°S–4°N averaged temperature at 17.5 km was initially 182.7 K. The CPT height is constant between 30°S and 30°N, in agreement with observations [Seidel et al., 2001]. The local maxima of northward (southward) winds are seen around 5°S (5°N) at the surface, and around 5°N (5°S) between 10 and 16 km. Strong upward winds are confined to between 5°S and 5°N, reaching ~14 km on average. These signals of meridional vertical wind indicate the Hadley circulation, with lower-level convergence and upper-level divergence near the equator.

[15] Figure 2 shows the longitude-time distribution of outgoing longwave radiation (OLR) averaged for 5°S–5°N using 7 km grid 3-hourly data. Large-scale eastward propagating organized clouds are remarkable in Figure 2. A cloud cluster is seen at 30°W–30°E on day 0 with a zonal scale of 3000 km; the cluster propagates globally at 17.5 m s<sup>-1</sup> and disappears at around 0° around day 28. Hereafter, we refer to this cluster as Super Cloud Cluster-A (SCC-A). Another large-scale organization, as large as SCC-A, appears at 90°W–60°W around day 14. We term this cluster SCC-B. As with SCC-A, the zonal phase speed of SCC-B is ~17.5 m s<sup>-1</sup>. SCC-B does not dissipate during the calculation.

[16] *Nasuno et al.* [2007] noted that SCC-B consists of westward propagating cloud clusters (CCs) with a zonal scale of ~500 km, being similar to the observed hierarchic structure of tropical convection [e.g., Nakazawa, 1988]. Around day 21, a mesoscale cloud system with a zonal scale of several hundred kilometers appears ~3000 km east of SCC-B and propagates eastward at 12 m s<sup>-1</sup>. The system reaches its mature stage around days 25–26, when 3.5 km

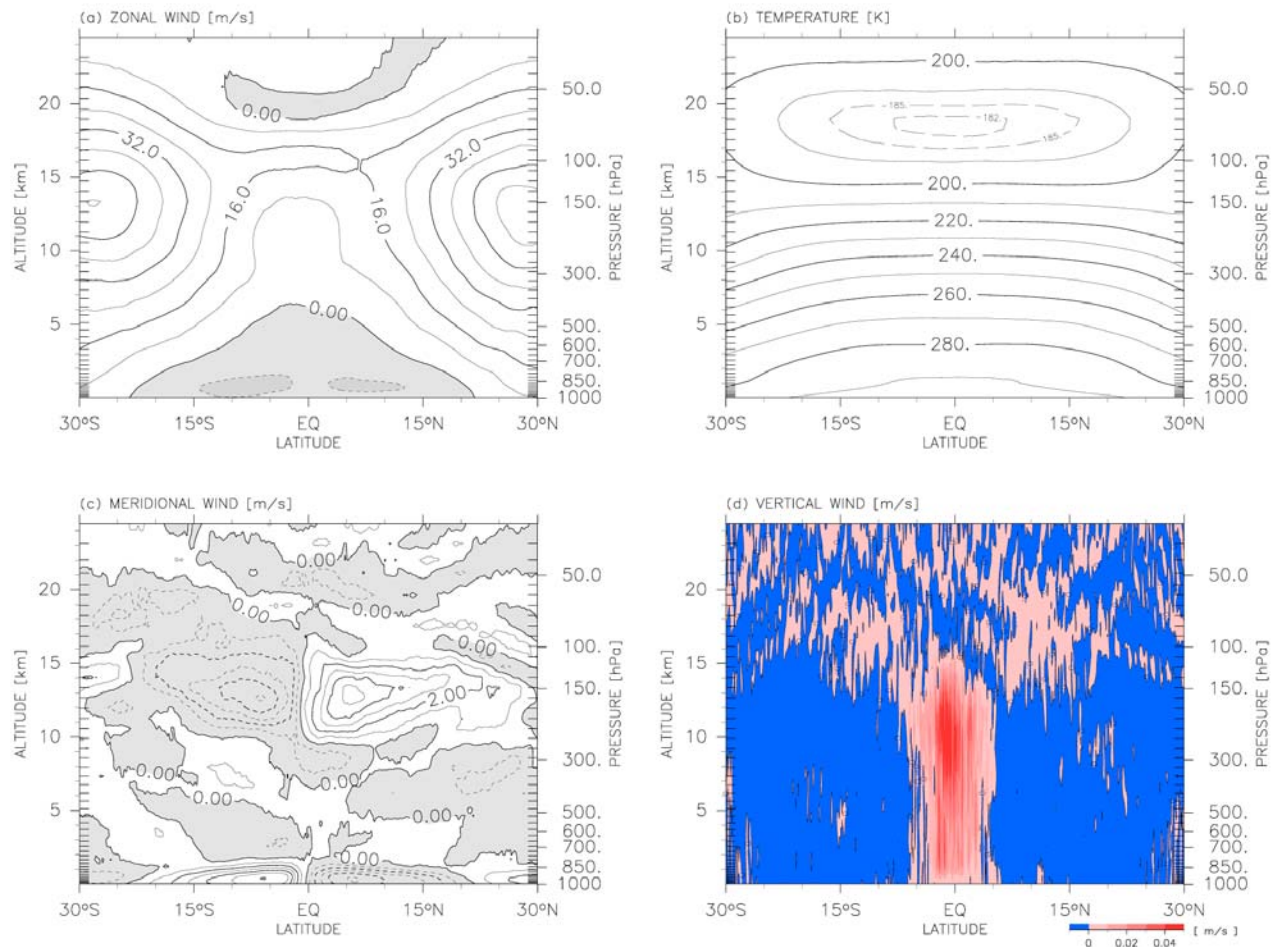


**Figure 1.** Latitude-altitude distributions of zonal mean (a) zonal wind, (b) temperature, (c) meridional wind, and (d) vertical wind from 3.5 km grid snapshot data. The contour intervals are  $8 \text{ m s}^{-1}$  for zonal wind,  $10 \text{ K}$  for temperature, and  $1 \text{ m s}^{-1}$  for meridional wind. Only the  $0 \text{ m s}^{-1}$  contour line is drawn for vertical wind. Shaded regions represent westward winds for zonal wind and southward winds for meridional wind. In the temperature profile, the 185 and 182 K lines are shown as dashed lines. Inner ticks upon vertical axes represent model levels. The pressure levels are approximate, calculated from the relation  $p = 1000 \exp(-z/H)$ , where  $p$  is pressure,  $z$  is altitude, and  $H = 7 \text{ km}$  is the scale height.

grid snapshot data are available. *Nasuno et al.* [2007] suggested that this cloud system is a well-organized squall-type cloud system, being categorized as a super convective system (SCS) as defined by *Chen et al.* [1996]. Therefore, we also refer to this system as an SCS.

[17] Figure 2 also shows the horizontal distribution of OLR using 3.5 km grid snapshot data at 0000 UT on day 25. Although the 3.5 km grid run is a free run with the initial conditions provided from the 7 km grid run on day 20, the tropical cloud distribution on day 25 is similar for both runs. Cloud systems corresponding to SCC-A, SCC-B, and the SCS are found around  $60^\circ\text{W}$ – $15^\circ\text{W}$ ,  $15^\circ\text{E}$ – $70^\circ\text{E}$ , and  $90^\circ\text{E}$ – $110^\circ\text{E}$ , respectively. If we take  $105 \text{ W m}^{-2}$  as a threshold OLR value for tall clouds, following *Chen et al.* [1996], the zonal scale of the SCS is  $\sim 1,100 \text{ km}$ . The SCS consists of two cumulonimbus clouds, and the minimum OLR value reaches  $\sim 60 \text{ W m}^{-2}$ .

[18] Figure 3 shows average profiles of temperature, potential temperature, vertical temperature gradient, and the frequency distribution of cloud top height for  $5^\circ\text{S}$ – $5^\circ\text{N}$ . The

cloud top height is defined as the highest (linearly interpolated) level at which the total condensates (including cloud ice, cloud water, rain, and snow) is equal to  $0.01 \text{ g kg}^{-1}$ , following *Grabowski* [1998]. The results obtained from 3.5 and 7 km grid data are generally in good agreement. The temperature and height of the CPT are 181.1 K and 18.2 km, respectively, and those of the lapse-rate tropopause (LRT: in short, the lowest level at which the lapse rate decreases to  $2^\circ\text{C km}^{-1}$  [e.g., *Seidel et al.*, 2001]) are 184.1 K and 17.9 km, respectively; the values obtained for lapse-rate tropopause are colder and higher, respectively, than the observed zonal mean tropical lapse-rate tropopause in March (191 K, 16.8 km). The standard deviation of temperature is  $\sim 2.2 \text{ K}$  between 16 km and 20 km for 7 km grid data. Using GPS satellite data between  $20^\circ\text{S}$  and  $20^\circ\text{N}$  in January 2006, *Gottelman and Birner* [2007] showed that the standard deviation of temperature at cold point tropopause is  $\sim 3.9 \text{ K}$ .

[19] The bottom boundary of the TTL, defined by the lapse rate minimum [e.g., *Gottelman and Birner*, 2007], is located at 11.2 km, and that defined by 350 K potential

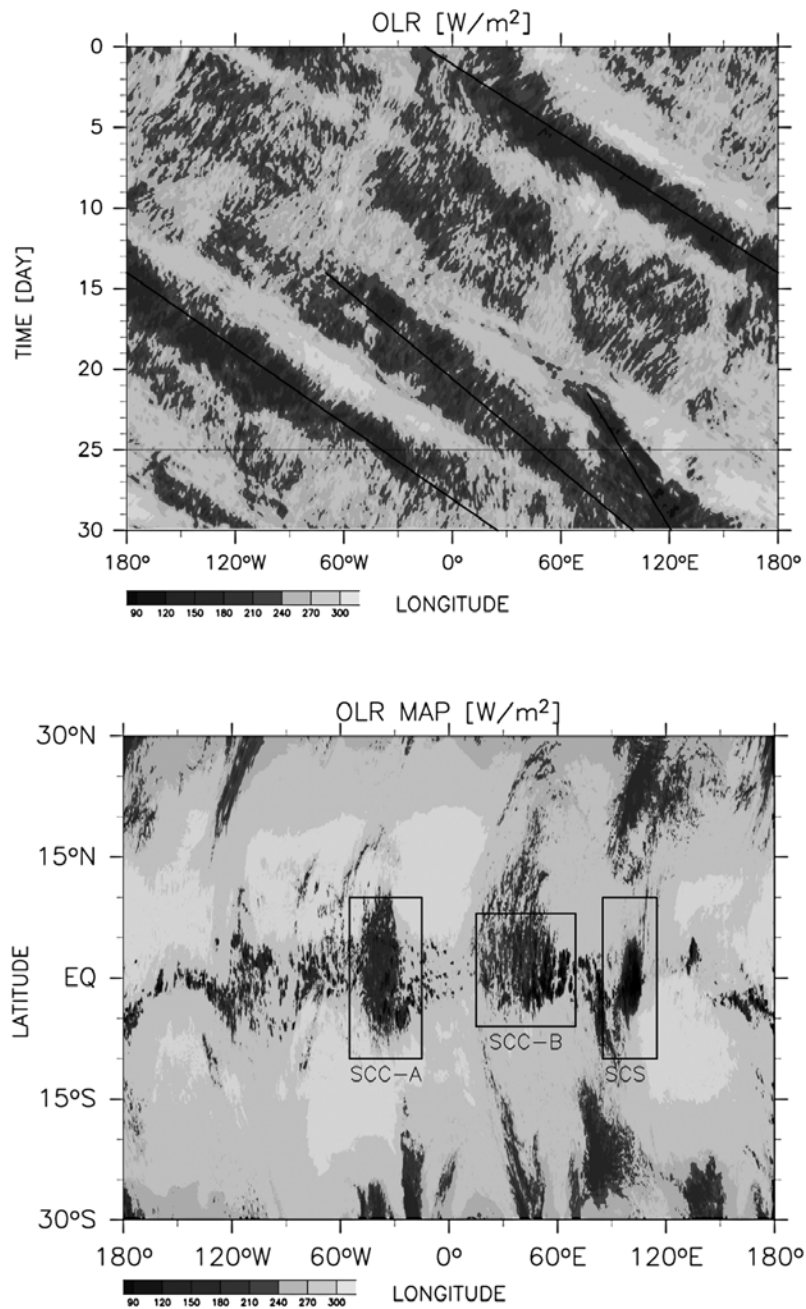


**Figure 2.** (top) Longitude-time distribution of outgoing longwave radiation (OLR) from 7 km grid 3-hourly data averaged between 5°S and 5°N. (bottom) Horizontal distribution of OLR at 0000 UTC on day 25, from 3.5 km grid snapshot data. The thick sloping lines in the top plot indicate the locations of organized convection (SCC-A, SCC-B, and SCS), whose counterparts are shown by rectangles in the bottom plot. The horizontal line in the top plot indicates the time slice shown in the bottom plot.

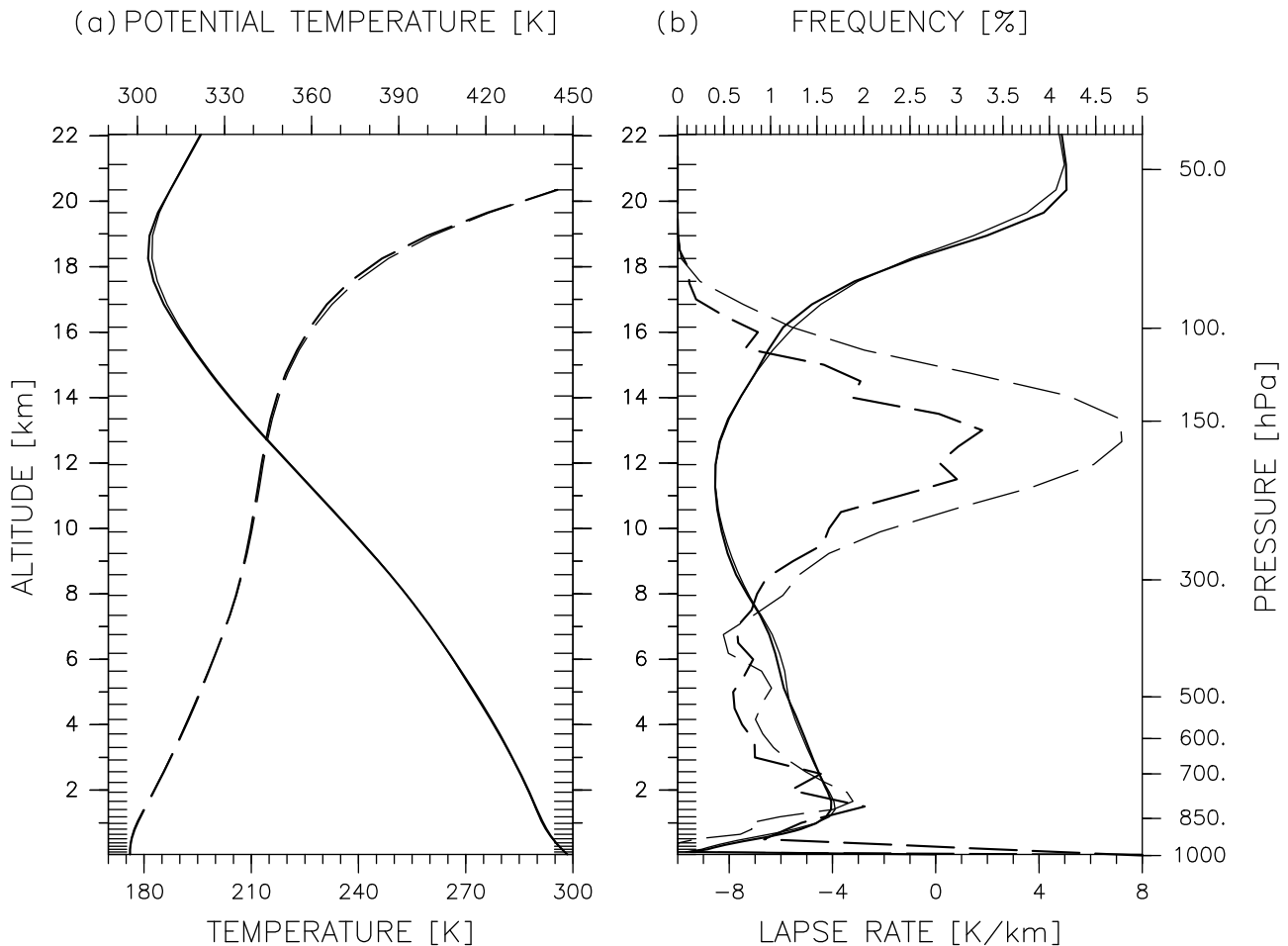


**Figure 3.** Average vertical distributions of (a) temperature (solid lines) and potential temperature (dashed lines) and (b) lapse rate (solid lines) and frequency of cloud top height (dashed lines) for the region 5°S–5°N. Thick and thin lines are derived from 3.5 km grid snapshot data and 7 km grid 30 day data, respectively.

temperature is located at 14.5 km. There exist two major maxima in cloud top height frequency, at 1–3 and 11–14 km. The former corresponds to the trade inversion, and the latter to the level of maximum convective outflow. A small maximum is observed around 5.5–6 km, slightly above the melting layer (0°C, at 4.9 km). This cloud top height distribution, with three maxima, may correspond to the observed trimodal structure in tropical convection, as discussed by Johnson *et al.* [1999].

[20] Figure 4 shows the probability density distribution for lapse-rate tropopause potential temperature and the boundary layer (35–1.9 km) equivalent potential temperature for 5°S–5°N. As discussed by Fueglistaler *et al.* [2009], the existence of an overlap between the two distributions provides an indirect indication that some clouds may reach the stratosphere. The overlap ratio in the present case is much lower than that obtained at Koror in the tropical western Pacific, as analyzed by Fueglistaler *et al.* [2009, Figure 13a]. Note that Fueglistaler *et al.* used Koror data for 1999–2004 in all seasons (I. Folkens, personal communication, 2009). Their method can result in a significant overestimate of the overshoot probability if, for example, there exists a difference between the season for lower lapse-rate tropo-

pause and the season for higher boundary layer equivalent potential temperature. Using our model data, we further investigated the ratio for the area where the boundary layer equivalent potential temperature is equal to or greater than the lapse-rate tropopause potential temperature at each grid point. We found that the ratio is zero for 3.5 km grid snapshot data and  $\sim 0.01\%$  for 7 km grid 30 day data. However, as discussed in section 4, the actual overshooting frequency estimated using direct cloud information is much higher than those estimated from boundary layer equivalent potential temperature.

## 4. Results and Discussion

### 4.1. Cloud Top Height Statistics

[21] The height distribution of tropical cumulonimbus clouds represents the key to evaluating the role of such clouds in dehydration of the TTL and lower stratosphere. If cumulonimbus clouds penetrating the bottom boundary of the TTL and even the cold-point tropopause are not rare, their impact can be substantial. In this section, cloud top height statistics are investigated using various model para-

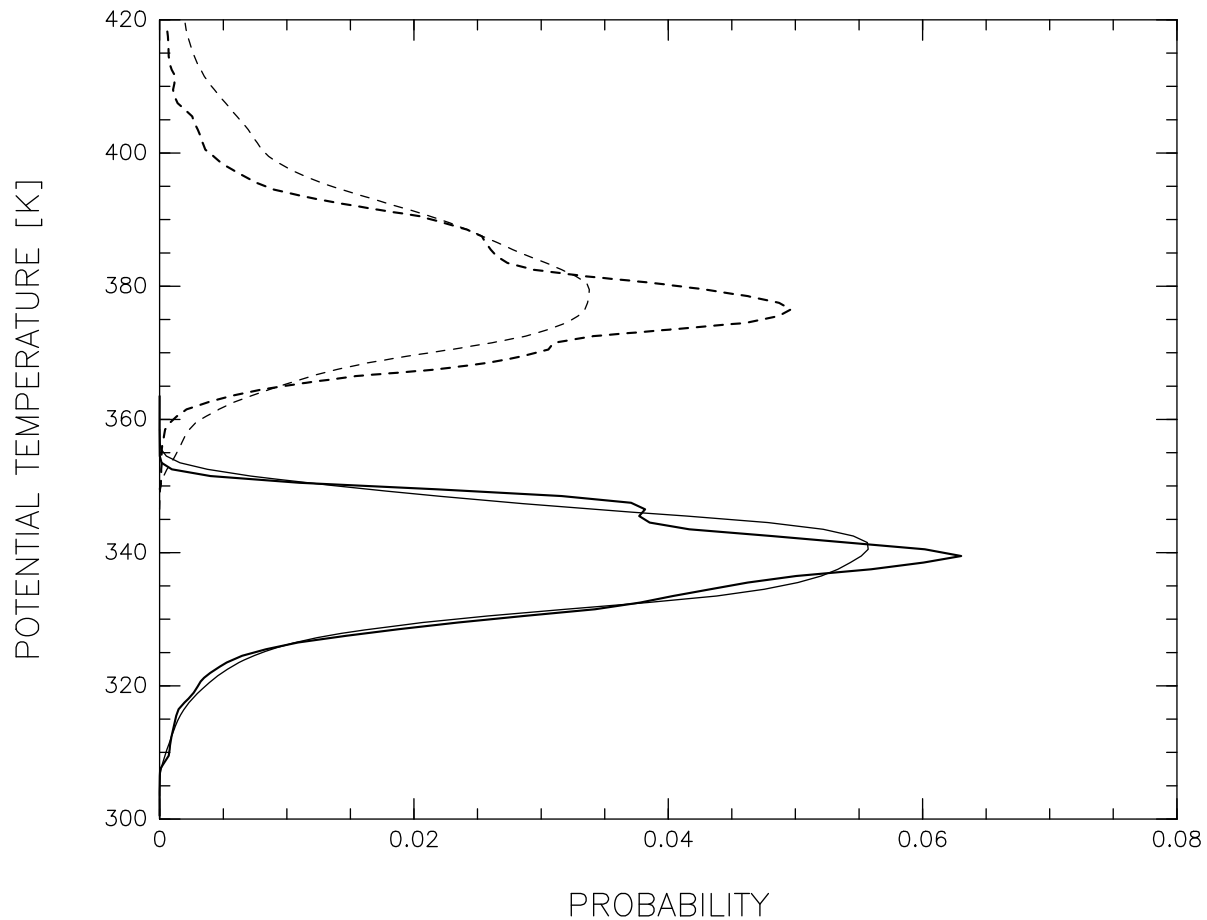


**Figure 4.** Probability density distribution for lapse-rate tropopause potential temperature (dashed lines) and boundary layer equivalent potential temperature (solid lines) for the region 5°S–5°N. The grid points for which the lapse-rate tropopause exceeds 22 km (<2%) are excluded. The boundary layer equivalent potential temperatures are used between 35 m and 1.9 km, within the planetary boundary layer. Thick and thin lines are derived from 3.5 km grid snapshot data and 7 km grid 30 day data, respectively.

meters, and are compared with the limited available observation data.

[22] Figure 5 shows the longitude-altitude distribution of cloud (defined as total condensates, including cloud ice, cloud water, rain, and snow) and the longitudinal distributions of lapse-rate tropopause and the TTL bottom boundary, defined as the lapse rate minimum averaged for 5°S–5°N using 3.5 km grid data. Many clouds overshoot into the TTL. The frequency of grid points with clouds penetrating the mean TTL bottom boundary (11.2 km) and the mean lapse-rate tropopause (17.9 km) is 25.3% and 0.14%, respectively (Figure 3). More than 90% of clouds that overshoot the mean lapse-rate tropopause are located in the region of SCC-B (15°E–70°E) and the SCS (90°E–110°E). Eighty percent of clouds whose top is located above 10 km have their base in the lower to middle troposphere. The tropopause shows large variations in longitude, particularly at 60°W–0°; this point is discussed in section 4.2.

[23] The bottom of the TTL is largely controlled by vertical mass flux associated with cumulus convection [e.g., *Folkins et al.*, 2000; *Folkins*, 2002]. Thus, the vertical frequency distribution of vertical wind velocity may provide further insight into the TTL structure in the model.

[24] Figure 6 shows vertical profiles of mass flux for clear sky regions and deep convective regions between 25°S and 25°N. Deep convective regions are defined as grid points where the cloud top is higher than 10 km and the cloud bottom is lower than 2.0 km; such regions are mainly located between 5°S and 5°N (Figure 2). The net downward mass flux in clear sky regions is largely balanced by net upward mass flux in convective regions. The local minimum (maximum) of mass flux for clear sky (convective) regions is found around ~8 km (400 hPa).

[25] Using data from the Tropical Ocean Global Atmosphere Coupled Ocean–Atmosphere Response Experiment (TOGA COARE) and a buoyancy-sorting cloud model, *Ciesielski et al.* [2003] showed that the local maximum of convective mass flux is located between 300 and 500 hPa. Above ~8 km, absolute values of mass flux in both regions decrease with altitude, and change their sign at ~16 km. This finding suggests that lower to middle tropospheric air is merely transported directly above ~16 km by convection. *Folkins* [2002] presented annually averaged clear-sky mass flux profiles for various latitude ranges, as calculated from clear-sky radiative heating profiles. Their result for 5°S–5°N indicates that the largest downward mass flux is located

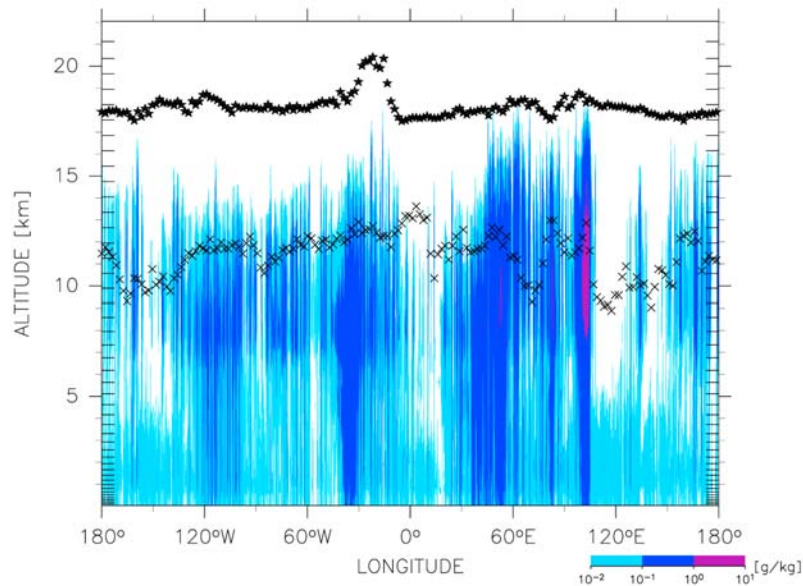


**Figure 5.** Longitude-altitude distribution (averaged over  $5^{\circ}\text{S}$ – $5^{\circ}\text{N}$ ) of total condensates (color scale), locations of the lapse-rate tropopause (stars), and locations of the bottom of the TTL (crosses) defined by the lapse rate minimum from 3.5 km grid snapshot data. Color scale regions correspond to those with total condensates greater than  $0.01 \text{ g kg}^{-1}$ . The number of symbols representing the tropopause and TTL bottom is reduced to one sixtieth of the model resolution.

around 345 K ( $\sim 11.3 \text{ km}$ ) and the level of zero mass flux is located around 356 K ( $\sim 15.0 \text{ km}$ ).

[26] Figure 7 shows the convective detrainment rate calculated from the clear-sky mass flux profile shown in Figure 6a (similar to Figure 1 of *Folkins et al.* [2006]). A mean entrainment is seen below  $\sim 7 \text{ km}$ , and a mean detrainment is seen above  $\sim 7 \text{ km}$  up to 17 km. Between 15 km and 17 km, a negative gradient is observed. This is qualitatively consistent with the result by *Folkins et al.* [2006].

[27] Figure 8 shows the frequency distribution of vertical wind. Strong vertical wind speeds ( $\geq 10 \text{ m s}^{-1}$ ) are only

found in upward winds, possibly directly associated with deep convection. The frequency curves for 0.8 and 1.6 show a sudden decrease with height within the TTL, particularly for upward winds. The curve for 0.8 crosses  $10 \text{ m s}^{-1}$  at  $\sim 16 \text{ km}$  for upward winds. Considering that in this model the mean horizontal wind at the equator in the TTL is  $\sim 15 \text{ m s}^{-1}$ , the 16 km level may represent some type of boundary for the mass flux.

[28] Next, we consider the latitudinal distribution of penetrating clouds. It should be noted that there exist several points (0.024% of the grid cells in the area  $5^{\circ}\text{S}$ – $5^{\circ}\text{N}$ ) where

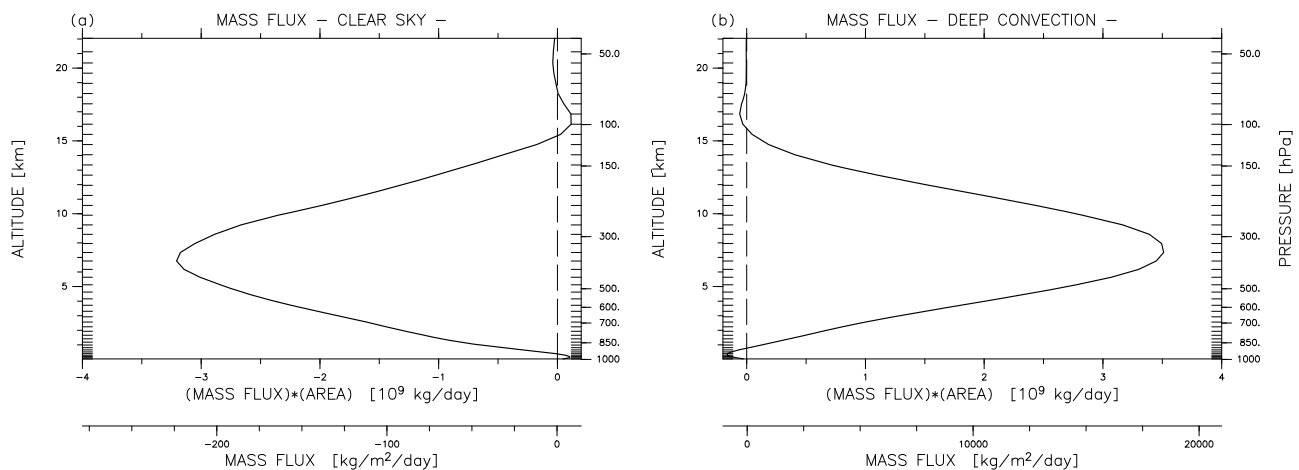


**Figure 6.** Vertical profiles of mass flux and mass flux multiplied by area for (a) clear-sky regions and (b) deep convective regions between  $25^{\circ}\text{S}$  and  $25^{\circ}\text{N}$  based on 3.5 km grid snapshot vertical wind and density data. Deep convective regions are defined as grid points for which the cloud top is above 10 km and the cloud bottom is below 2.0 km.

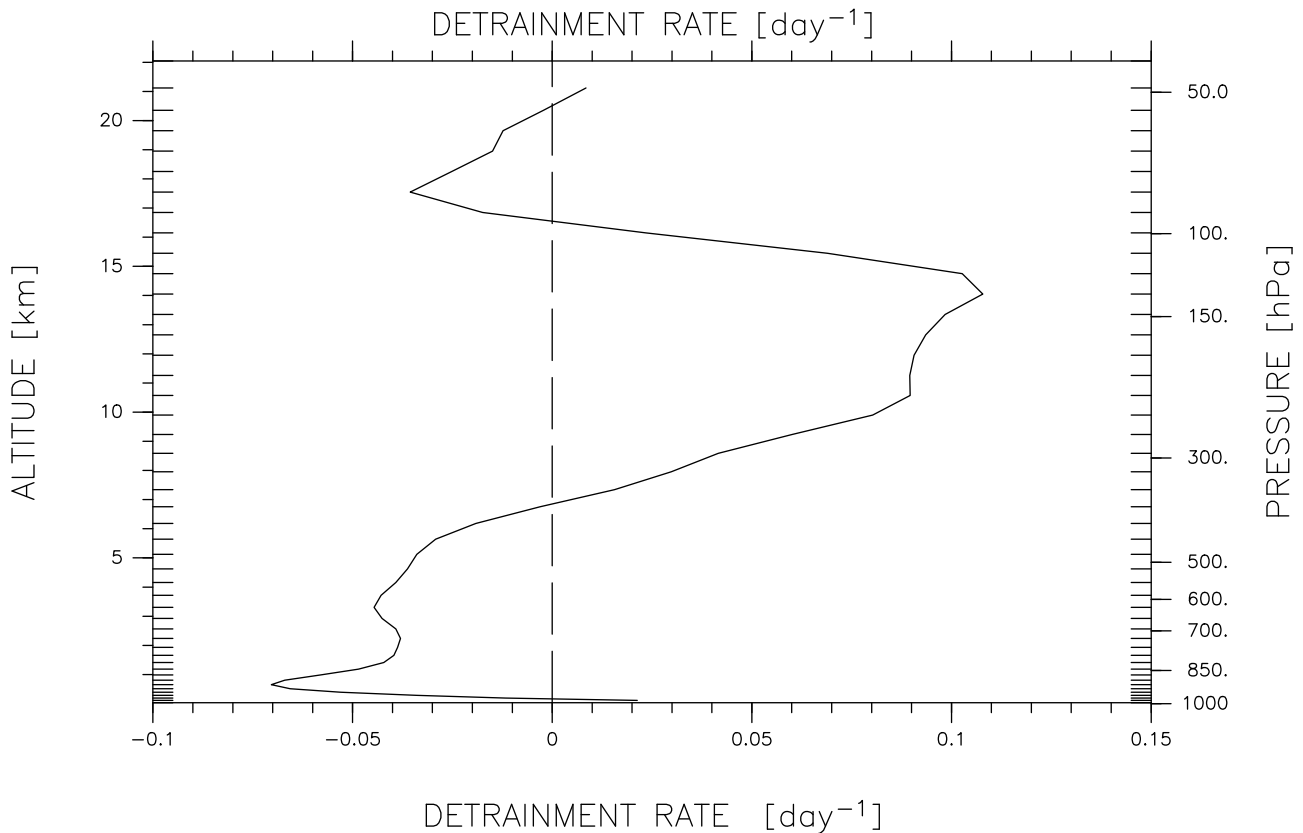


**Figure 7.** The convective detrainment rate calculated from the clear-sky mass flux profile shown in Figure 6a.

the bottom of TTL, as defined by the lapse rate minimum, is located above the mean lapse-rate tropopause at 17.9 km. This results from the influence of large-amplitude equatorial Kelvin waves (see section 4.2). We excluded these points from the frequency calculations. Figure 9 shows the latitudinal frequency distribution of the cloud top located in the stratosphere and in the TTL, where the cloud top height is again defined as 0.01 g kg<sup>-1</sup> total condensates. We also show the frequency of cumulonimbus penetration by applying an additional condition (i.e., the cloud base being located within the planetary boundary layer). For 3.5 km grid data, the maximum frequency is seen at ~2°S for stratospheric penetration and at ~1°S for TTL penetration. These high clouds are located mainly in the SCC-B and SCS regions. The frequency of TTL penetration decreases with increasing latitude, and tropopause overshooting does not occur outside the 5°S–3°N region. For 7 km grid data at 0000–0300 UT on day 25, the maximum frequency of stratospheric penetration is seen at the equator, and decreases with increasing latitude; a similar trend is observed for TTL penetration, although with a maximum frequency at 2°S. The difference in the peak location of stratospheric penetration between 3.5 and 7 km grid data reflects the slightly different structures of SCC-B and the SCS. For 7 km grid data with a 30 day average, the maximum frequency is seen at the equator for both stratospheric and TTL penetration, decreasing with increasing latitude. The differences between Figures 9a and 9c and between Figures 9b and 9d reflect the existence of cirrus, anvil, and stratus. We found

that in the 3.5 km grid data, cirrus with a thickness  $\leq 1$  km (2 km) occur in 13.1% (25.5%) of the 5°S–5°N region above 10 km.

[29] In our model, for 3.5 km grid data, the lapse-rate tropopause penetration for 5°S–5°N is 0.17%; for 7 km grid data, the equivalent value is 0.25%. Using the GLAS ICESat data, *Dessler et al.* [2006] show that overshooting frequency is 0.34% in the tropics. The overshooting frequency from our results is slight lower than that obtained from observations by *Dessler et al.*, [2006]. We note once again that the overshooting frequency estimated from potential temperature, as discussed in section 3, does not correspond to the actual overshooting frequency in our aqua planet experiments. One possible reason for this discrepancy is that in section 3 we did not consider the time taken for boundary layer air to reach the tropopause; potential temperatures should have been compared along the same in-cloud trajectories.

## 4.2. Major Disturbances in the TTL

### 4.2.1. Equatorial Kelvin Waves

[30] Figure 10 shows the horizontal distribution of lapse-rate tropopause height using 3.5 km grid snapshot data. We observe a region with very high tropopause at 30°W–15°W, 10°S–15°N, with a ~3 km drop at ~15°W. The tropopause over other tropical regions (including 15°E–110°E) where SCC-B and the SCS exist shows no significant large-scale variations.

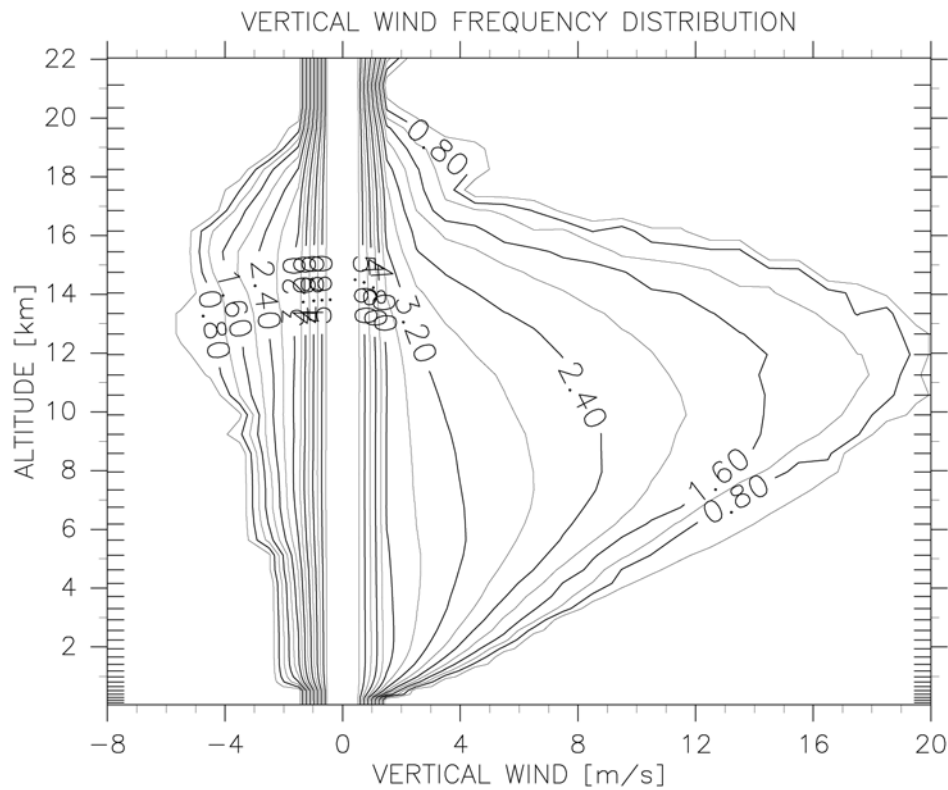


**Figure 8.** Frequency distributions of vertical wind in the region 5°S–5°N, from 3.5 km grid snapshot data. Contours represent the log base 10 of the number of grid points in each  $\Delta w = 1 \text{ m s}^{-1}$  bin at each altitude level. The contour interval is 0.4.

[31] Figure 11 shows the longitude-altitude distributions of total condensates and temperature anomaly from the zonal mean, together with the lapse-rate tropopause locations at the equator (0.018°N). Convection associated with SCC-A can be seen around 50°W–30°W, and a clear gap in the tropopause is found at  $\sim 15^\circ\text{W}$ . The high tropopause west of 15°W corresponds to the boundary between a warm anomaly below and a cold anomaly above, while the low tropopause east of 15°W corresponds to a cold anomaly around the lapse-rate tropopause. These temperature anomalies in the TTL are closely related to SCC-A. We observe two tilted cold anomalies around SCC-A: one from 60°W at 13 km through 15°W at 15 km and further east, and the other from 60°W around 8 km through 0° at 6 km and further east. A warm anomaly is located between these two cold anomalies, east of SCC-A. These observations are characteristic of convectively coupled equatorial Kelvin waves, as discussed by *Wheeler et al.* [2000].

[32] Figure 12 shows the phase relationship between temperature and zonal wind for TTL disturbance. At 18.2 km, the warm anomaly is centered at  $\sim 30^\circ\text{W}$ , while the eastward wind anomaly is centered at  $\sim 50^\circ\text{W}$  and the westward wind anomaly is centered at  $\sim 10^\circ\text{W}$ . The center of the cold anomaly is unclear. If we focus on the warm anomaly and zonal wind “wave packet” at 60°W–0°, which are moving eastward (Figure 13), we observe that the temperature anomaly leads the zonal wind anomaly by a quarter cycle. Furthermore, the meridional wind component is

negligible near the equator, and the zonal wind distribution is symmetrical about the equator.

[33] Figure 13 shows the longitude-time distribution of temperature anomaly averaged for 5°S–5°N, at 18.2 km. The solid lines in Figure 13 represent the tracks of organized convection, SCC-A, SCC-B, and the SCS (see Figure 2). Signals propagating eastward at  $24 \text{ m s}^{-1}$  are clearly seen; these are slightly faster than SCC-A. The dispersion relation of equatorial Kelvin waves is  $\omega = k\bar{u} - Nk/m$ , where  $\omega$ ,  $k$ ,  $\bar{u}$ ,  $N$ , and  $m$  are frequency, zonal wave number, background zonal wind, buoyancy frequency, and vertical wave number [*Andrews et al.*, 1987], respectively. Zonal wavelength ( $2\pi/k$ ) is estimated as 12,000 km, vertical wavelength ( $2\pi/m$ ) as 8 km,  $\bar{u}$  as  $8.9 \text{ m s}^{-1}$ , and  $N$  as  $2.36 \times 10^{-2} \text{ s}^{-1}$ . These values are taken from day 8 (0000 UT) in the 7 km grid data (not shown). Note that zonal mean zonal wind is used as the background wind. The period ( $2\pi/\omega$ ) is  $\sim 6$  days (see Figure 13, from the warm phase at day 7 to the cold phase at day 10, along 120°E), corresponding to  $\omega$  of  $1.2 \times 10^{-5} \text{ s}^{-1}$ . These values reasonable satisfy the dispersion relation of equatorial Kelvin waves, and are characteristic of equatorial Kelvin waves [e.g., *Parker*, 1973]. Similar to the cases discussed by *Fujiwara and Takahashi* [2001] and *Fujiwara et al.* [1998, 2009], organized convection associated with SCC-A in the present case generates a dry Kelvin wave packet in the TTL. It is important to note that individual cumulus clouds simulated in these experiments are organized to form large-scale waves in the TTL; cloud organization may therefore be more important than indi-

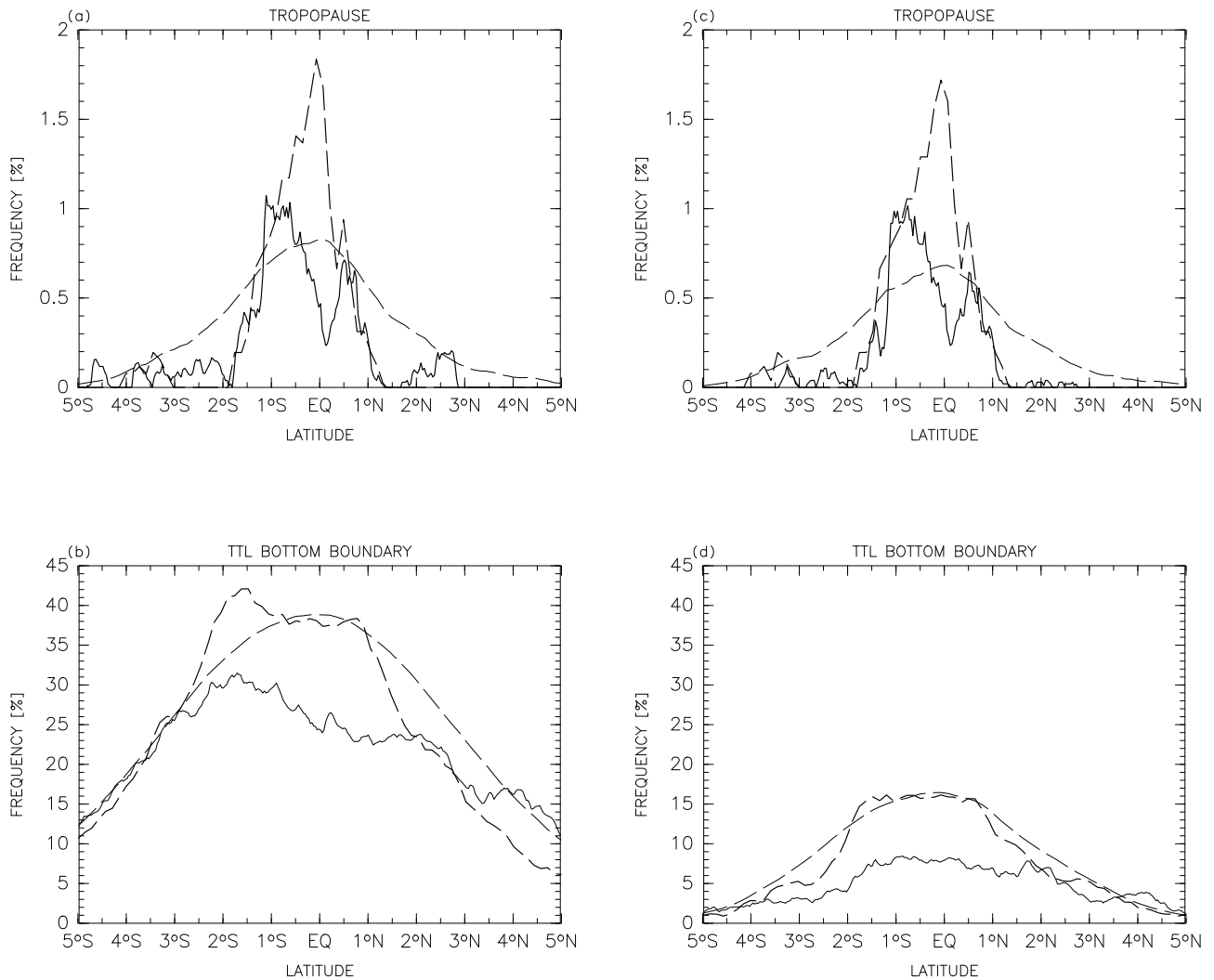


**Figure 9.** Latitudinal distributions of the frequency of clouds located (a) above the local lapse-rate tropopause and (b) above the local TTL bottom boundary defined by the lapse rate minimum, using 3.5 km grid snapshot data (solid lines), 7 km grid data on day 25 at 0000 UT (thick dashed lines), and 30 day data (thin dashed lines). (c) As in Figure 9a but for clouds with a base located below 1.9 km (i.e., within the boundary layer). (d) As in Figure 9b but for clouds with a base located below 1.9 km.

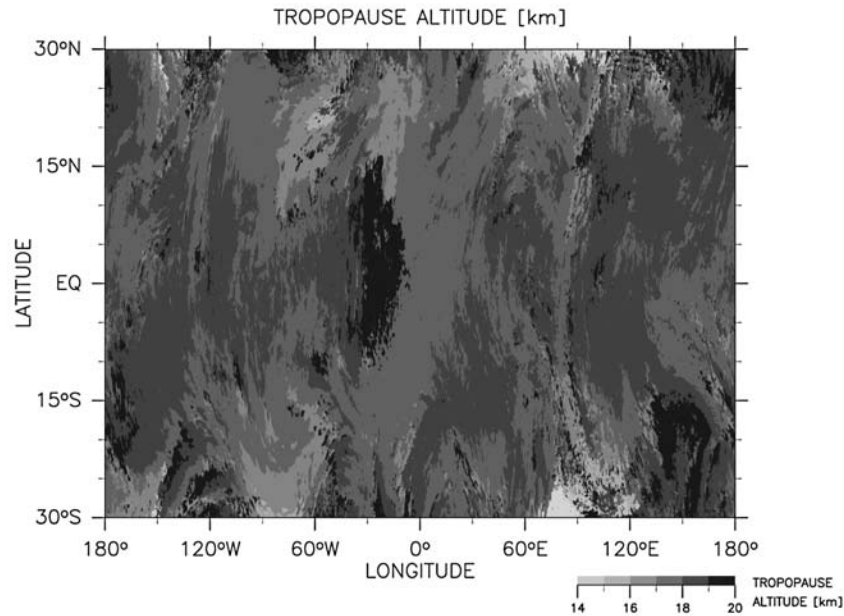


**Figure 10.** Horizontal distribution of lapse-rate tropopause height, based on 3.5 km grid snapshot data.

vidual cumulus clouds for the TTL in terms of dehydration within the TTL.

#### 4.2.2. Gravity Waves Superimposed on the Cold Phases of Kelvin Waves

[34] We found a very cold area ( $\leq 174$  K) in a cold phase of Kelvin waves, at around  $49.5^\circ\text{E}$ ,  $0.5^\circ\text{N}$  (Figure 12). Figure 14 shows a horizontal map of temperature and horizontal winds, focusing on this cold area. Horizontal wind divergence is observed in this region, and the meridional wind component is as strong as the zonal wind component. Figure 14 also shows the longitude-altitude distribution of potential temperature and zonal-vertical wind vectors along  $0.5^\circ\text{N}$  around the tropopause. We observe an upward air displacement that results in adiabatic cooling at  $48^\circ\text{E}$ – $56^\circ\text{E}$  and 17–19 km. In this region, no deep convective clouds extend above 16 km. At  $46^\circ\text{E}$ – $48^\circ\text{E}$ , we see downward air displacement with a similar magnitude to that of the upward air. Focusing on the 370 K potential temperature contour at  $46^\circ\text{E}$ – $52^\circ\text{E}$ , we observe a wave signal with a zonal wavelength of  $\sim 600$  km. The wave form departs from sinusoidal, the amplitude is very large, and the air is neutrally stratified at  $49^\circ\text{E}$ ; these features are characteristic of large-amplitude, breaking gravity waves. In fact, vertical profiles of zonal wind and meridional wind at  $46^\circ\text{E}$ – $52^\circ\text{E}$  clearly show a quadratic phase difference at 16–22 km (not shown); based on the hodograph, the vertical wavelength is estimated to be  $\sim 3$  km. The amplitudes of the temperature, and zonal and meridional wind components are 1.8 K,  $4.8 \text{ m s}^{-1}$ , and  $3.6 \text{ m s}^{-1}$ , respectively. Further analysis of the wind data suggests that wave energy is propagating westward and upward. The period relative to the ground is estimated to be  $\sim 3$  h, based on the dispersion relation of gravity waves,  $\omega = k\bar{u} - Nk/m$ . The gravity waves discussed above are probably generated from SCC-B. Because SCC-B is located to the east of SCC-A, which generated large-amplitude Kelvin waves in the TTL, the gravity waves generated by SCC-B encounter the

cold phase of Kelvin waves at the tropopause level, resulting in very cold temperatures. Pfister *et al.* [1993] observed gravity waves superimposed on large-scale disturbances around the tropopause, based on Stratosphere-Troposphere Exchange Project (STEP) data. Fujiwara and Takahashi [2001, Plate 1] observed a similar relationship (i.e., two large-scale convective organizations and large-amplitude Kelvin and gravity waves in the TTL) in an AGCM experiment. If this is a general relationship, the gravity waves superimposed on the cold phases of Kelvin waves may represent an important dehydration process in the tropical stratosphere.

#### 4.2.3. Structure of SCS

[35] Figure 15 shows a close look at an SCS using 3.5 km grid snapshot data. The SCS ranges from  $95^\circ\text{E}$  to  $106^\circ\text{E}$ , and from  $4^\circ\text{S}$  to  $5^\circ\text{N}$ . The highest cloud top is located at  $19.6 \text{ km}$  at  $101.3^\circ\text{E}$ ,  $1.21^\circ\text{S}$ , while the tropopause height at this point is  $18.5 \text{ km}$ ; therefore, the cloud overshoots the tropopause by about 1 km. The tropopause height in the region between  $100^\circ\text{E}$  and  $105^\circ\text{E}$  (the core of the SCS) is  $17 \text{ km}$ , lower than the height for the rest of the SCS region ( $18 \text{ km}$ ). In the core region, the lapse-rate tropopause temperature is also lower, attaining a minimum  $173.2 \text{ K}$  at  $103.2^\circ\text{E}$ ,  $0.018^\circ\text{N}$ . At  $18 \text{ km}$  and between  $100^\circ\text{E}$  and  $105^\circ\text{E}$ , the temperature is warmer than that of the rest of the SCS region. These tropopause features are discussed below. Figure 15 also shows vertical profiles of in-cloud properties at  $103.2^\circ\text{E}$ ,  $0.018^\circ\text{N}$ . The in-cloud temperatures at 5–16 km are higher than the zonal mean temperature because of latent heat release. The in-cloud temperature at 17–21 km has two local minima. The dry adiabatic lapse rate is only seen at around  $17 \text{ km}$ . The lapse rate at around  $20 \text{ km}$ , at the upper minimum, is  $-1^\circ\text{C km}^{-1}$ , much larger (and weaker) than the adiabatic lapse rate. These results suggest that the lower minimum is directly caused by deep convection, while the upper minimum may be due to gravity waves. We also

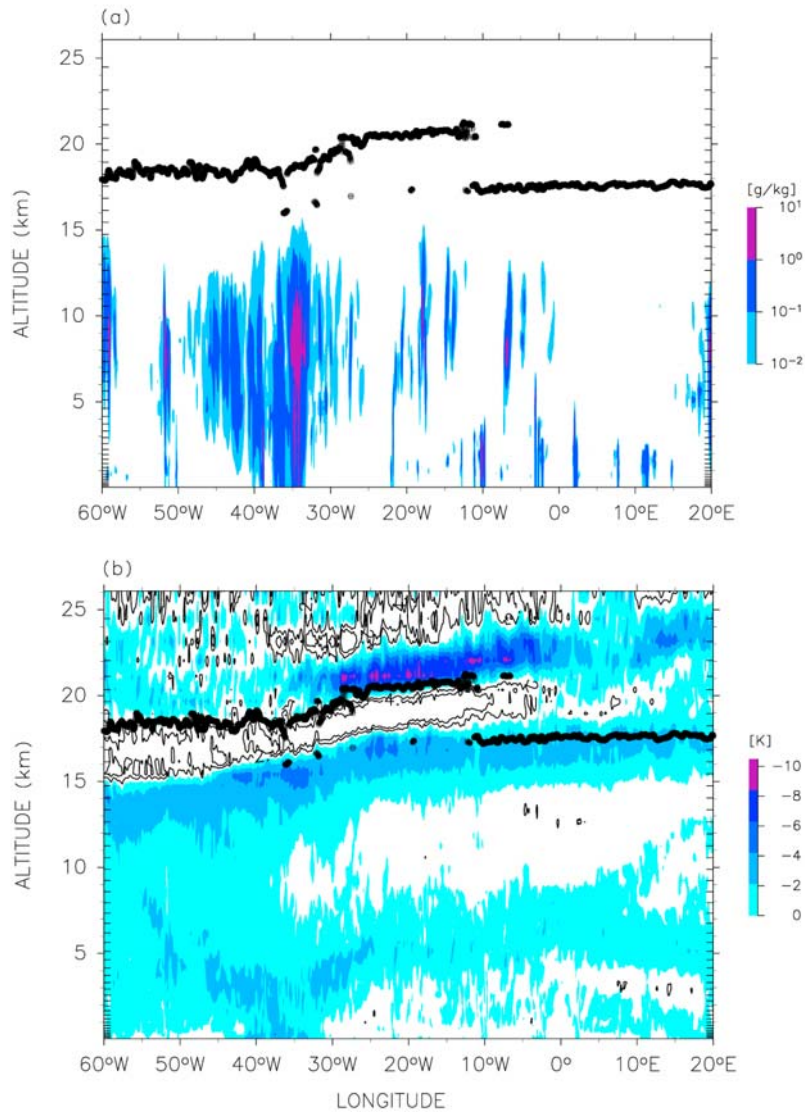


**Figure 11.** Longitude-altitude distributions of (a) total condensates and (b) temperature anomaly from the zonal mean at  $0.018^\circ\text{N}$  between  $60^\circ\text{W}$  and  $20^\circ\text{E}$  using 3.5 km grid snapshot data. For total condensates, the regions with values greater than  $0.01 \text{ g kg}^{-1}$  are colored. For the temperature anomaly, only those regions with negative values are colored, and the 0 and 4 K contours are shown. Locations of the lapse rate tropopause are shown by black symbols in Figures 11a and 11b.

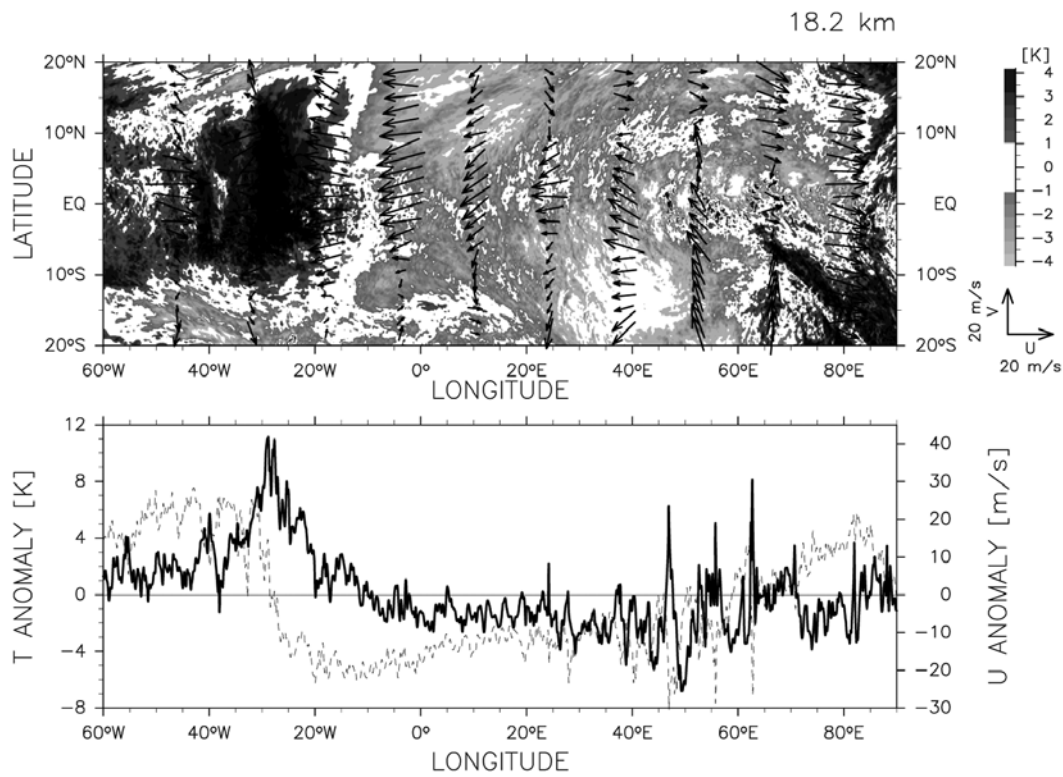


**Figure 12.** (top) Horizontal distribution of temperature anomaly (gray) and horizontal wind anomaly (vectors) from the zonal mean at 18.2 km using 3.5 km grid snapshot data. (bottom) Longitudinal distribution of temperature (T) anomaly (solid line) and zonal wind (U) anomaly (dashed line) from the zonal mean at 0.018°N and 18.2 km using 3.5 km grid snapshot data.

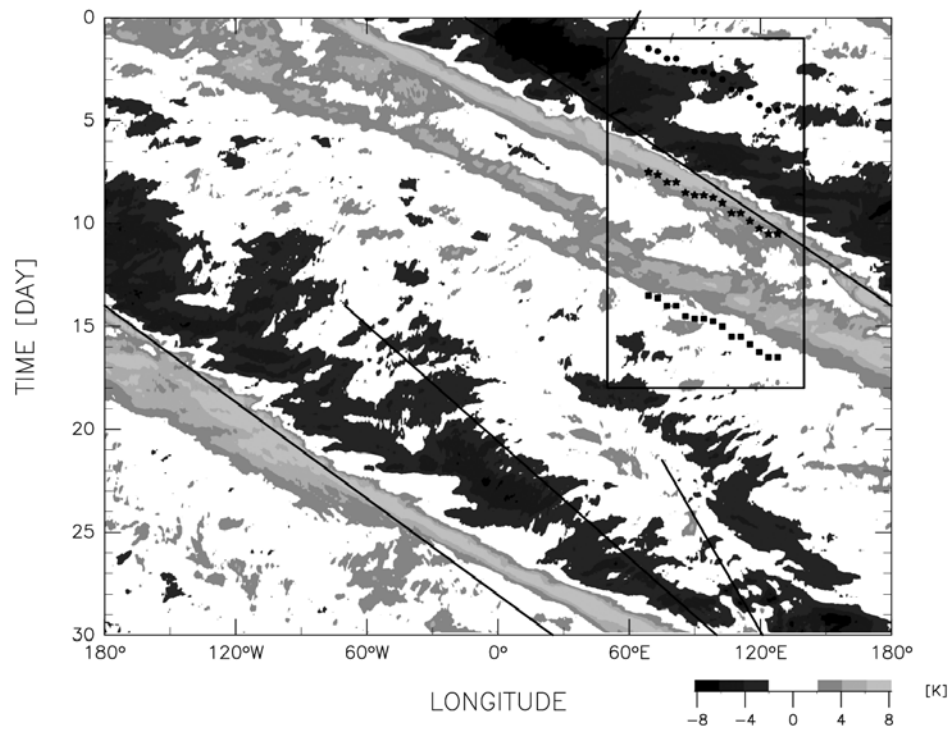


**Figure 13.** Longitude-time distribution of temperature anomaly from the zonal mean averaged for the region  $5^{\circ}\text{S}$ – $5^{\circ}\text{N}$  at 18.2 km using 7 km grid 3-hourly data. The solid sloping lines correspond to those in Figure 2 (top). In the “Kelvin-wave” region outlined by the rectangle, the locations of lag days 0, –6, and +6 for the composite shown in Figure 17 are indicated by stars, circles, and squares, respectively.

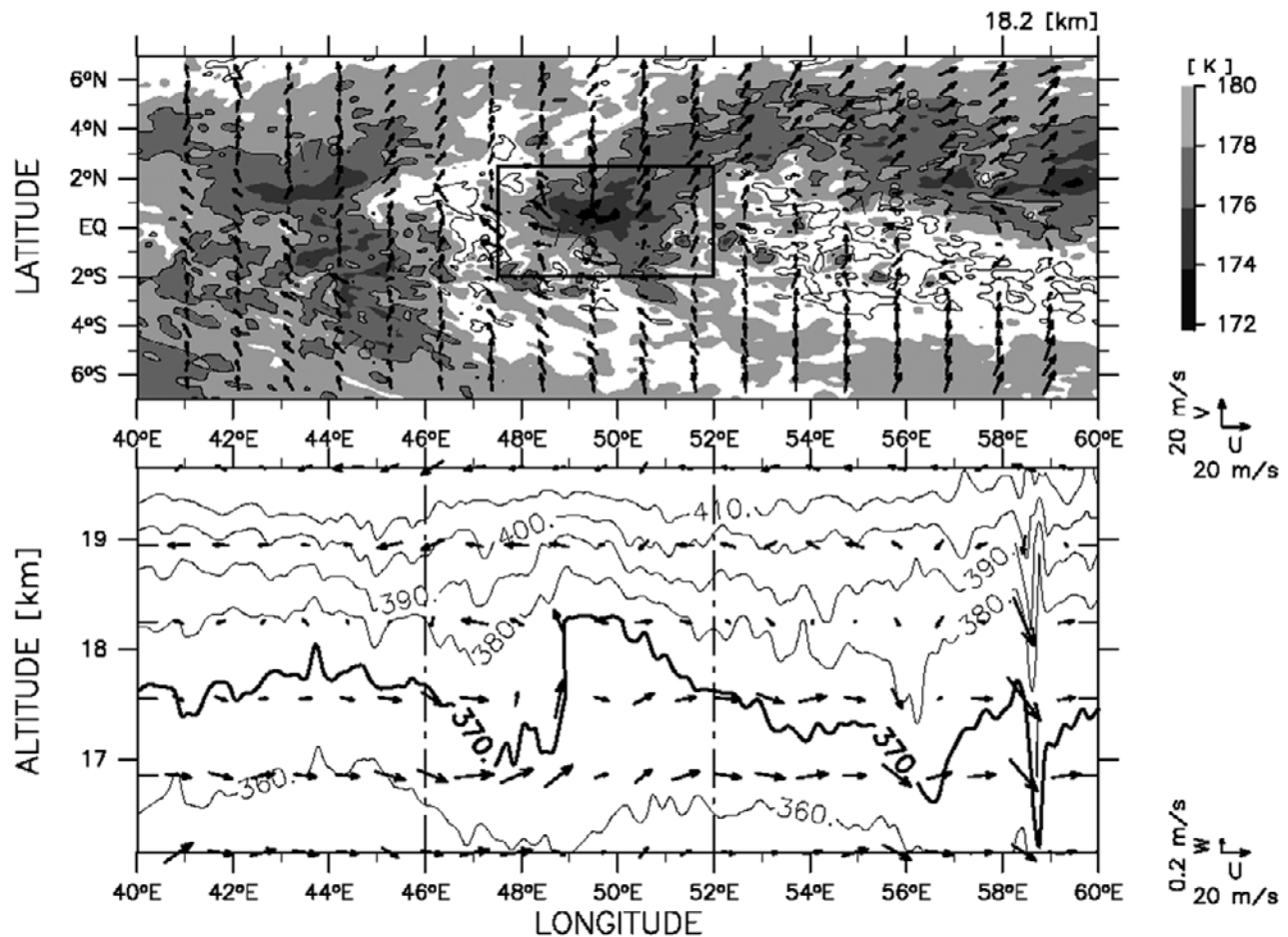


**Figure 14.** (top) Horizontal distribution of temperature (gray) and horizontal wind (vectors) at 18.2 km using 3.5 km grid snapshot data. (bottom) Longitude-altitude distribution of potential temperature (contours) and zonal-vertical wind (vectors) at 0.5°N using 3.5 km grid snapshot data. Regions with temperatures below 180 K are shaded gray, and the 178 K contour line is shown. The number of vectors in each plot is reduced to just 1 of every 25 in the horizontal.

observe that vertical wind is strongest ( $\sim 4.3 \text{ m s}^{-1}$ ) at around 14 km, but approaches  $0 \text{ m s}^{-1}$  at around 18 km. Above 18 km, vertical profiles of zonal and meridional winds show a marked quadratic phase difference (not shown), indicating the existence of inertia-gravity waves with a vertical wavelength of  $\sim 3 \text{ km}$ . Based on the dispersion relation theory of gravity waves with zonal wavelength, background zonal wind, and buoyancy frequency of 1000 km,  $8.4 \text{ m s}^{-1}$ , and  $0.02 \text{ s}^{-1}$ , respectively, the period is estimated to be  $\sim 15 \text{ h}$ . At this grid point, the cloud top height is 18.9 km, and the gravity waves caused a warm anomaly above 19 km due to their downward winds. These downward motions may have suppressed convective overshooting and directly influenced cloud particles in the lower stratosphere.

[36] In this section, we analyzed the in-cloud properties of an SCS using 3.5 km grid snapshot data. Such gigantic cloud systems were observed over the Indo-Pacific oceanic warm pool by *Chen et al.* [1996]. We found that clouds overshoot the tropopause by  $\sim 1 \text{ km}$  and moisten the TTL, at least at that time. We also found that downward motions associated with gravity waves, as generated by the SCS,

may prevent the cloud top from deeply penetrating the lower stratosphere. This finding suggests the need to consider detailed, complex cloud and wave dynamics to understand the cumulus overshooting process.

### 4.3. Water Vapor in the TTL

[37] Because of insufficient model integration time (90 days) and very dry initial lower stratosphere of the experiment, the stratospheric water vapor was found not to attain equilibrium at the time of analysis. Therefore, we investigate short-term variability in TTL water vapor and its cause, based on the NICAM aqua planet 7 km grid experiment in this section.

[38] Figure 16 shows the longitude-time distribution of water vapor mixing ratio at 18.2 km. Dry signals propagating eastward at  $\sim 24 \text{ m s}^{-1}$  are clearly seen. A broad dry signal exists between  $170^\circ\text{W}$  and  $60^\circ\text{W}$  on day 0, and propagates eastward at  $\sim 24 \text{ m s}^{-1}$  until day 30. At around day 15, there appears another eastward moving dry signal. Referring to the tropopause temperature field in Figure 13, we observe that the dry signals correspond to the warm

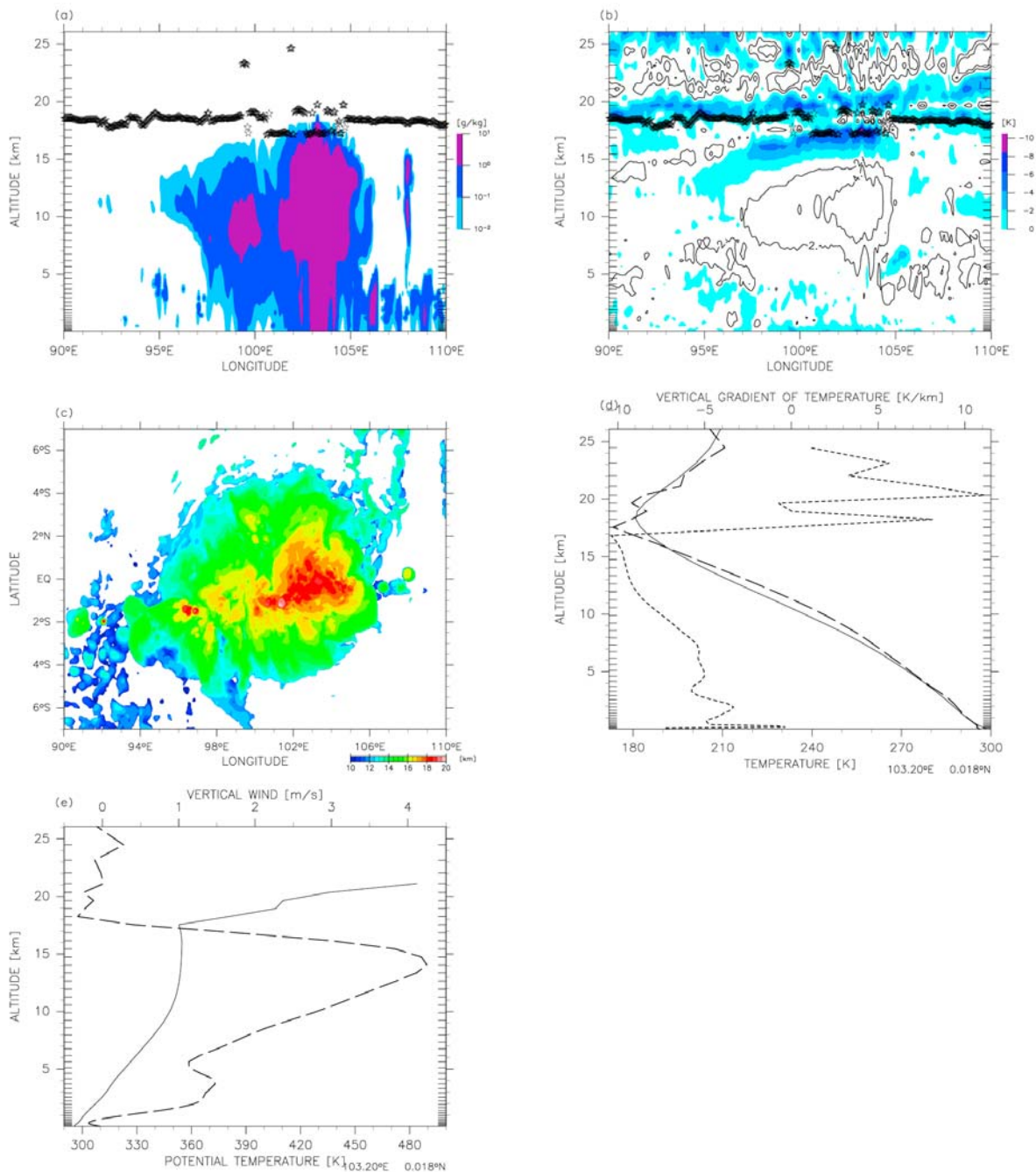


**Figure 15.** (a and b) As in Figures 11a and 11b but for 90°E–110°E using 3.5 km grid snapshot data. (c) Horizontal distribution of cloud top height using 3.5 km grid snapshot data in the region 7°S–7°N, 90°E–110°E. (d) Vertical profiles of temperature (long-dashed line) and vertical temperature gradient (short-dashed line) at 103.2°E, 0.018°N, and of the zonal mean temperature (solid line) at 0.018°N, using 3.5 km grid snapshot data. (e) Vertical profiles of potential temperature (solid line) and vertical wind (dashed line) at 103.2°E, 0.018°N.

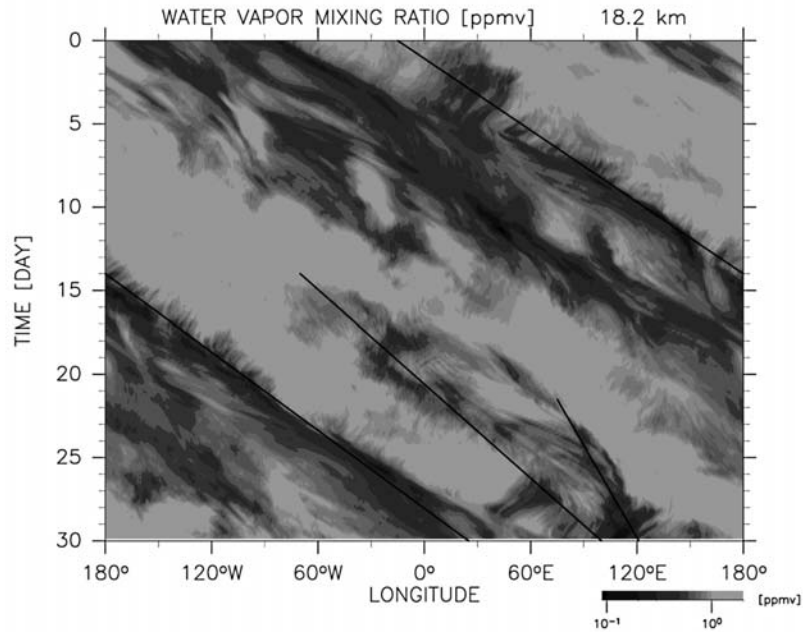


**Figure 16.** Longitude-time distribution of water vapor mixing ratio averaged for the region 5°S–5°N at 18.2 km using 7 km grid data. The sloping solid lines correspond to the tracks of super cloud cluster-A (SCC-A), super cloud cluster-B (SCC-B), and super convective system (SCS), as in Figure 2 (top) and Figure 13.

phases of Kelvin waves. Because these dry signals are the prominent feature in the water vapor field around the tropopause in this model, and because this type of large-scale disturbance is an important process in the real world, we investigated the eastward propagating dry signals in more detail by undertaking a composite analysis. The composite was constructed by taking the composite center (lag zero) at the time +2 K temperature anomaly appearing in the Kelvin-wave area at 60°E–120°E (see the area outlined by the rectangle in Figure 13). Next, we took the period from day –6 to day +6 as the composite lag days, and obtained time series data (at 3 h intervals) at each longitude (from 65°E to 130°E; at intervals of 0.14°; 462 points in total). Note that the selected area includes two warm signals (Figure 13). Figure 17 shows the composite results; i.e., the time-altitude distributions of temperature, potential temperature, zonal-vertical wind vector, and water vapor mixing anomaly. It is evident that the dry anomaly at lag time days 0–2 and at 16.5–19 km is located not at the cold phase of Kelvin waves but at the warm, downward displacement phase. This means that dry air is produced via dry air transport from the tropical lower stratosphere rather than via condensation processes. This is because the tropopause water vapor has not attained equilibrium and is too dry in this experiment. The dry air transport in the warm phases of Kelvin waves itself is an

important drying process in the TTL, as observed by *Fujiwara et al.* [2001, 2009].

## 5. Concluding Remarks

[39] We investigated various features of the TTL using a global, nonhydrostatic atmospheric model, NICAM, calculated at horizontal grid intervals of 3.5 and 7 km under an aqua planet condition. Large-scale organized convection with realistic hierarchical structures is observed around the equator in the model outputs.

[40] The frequency distribution of cloud top height contains two major maxima: around the top of the planetary boundary layer and at around 11–14 km. The latter corresponds to the level of maximum convective outflow, which determines the bottom of the TTL. At 5°S–5°N, we found that clouds reach the TTL in 25.3% of the area and that clouds overshoot the mean lapse-rate tropopause level (17.9 km) in 0.14% of the area. These results suggest that cumulus clouds can play a major role in dehydration within the TTL. We also investigated tropical vertical wind statistics that may characterize direct convective mass flux into the TTL. We found that ~16 km is the level at which very strong upward winds ( $\sim 10 \text{ m s}^{-1}$ ) cease to exist. The latitudinal frequency distribution of clouds overshooting the

**Figure 17.** Time-altitude distributions of (a) temperature (gray scale), potential temperature (contours), and zonal-vertical wind (vectors) and (b) water vapor mixing ratio anomaly (gray scale) and potential temperature (contours). The shaded regions for water vapor mixing ratio correspond to values less than  $8 \times 10^{-1}$  ppmv. (c) Time-averaged (from day –6 to day +6) vertical distribution of water vapor mixing ratio.

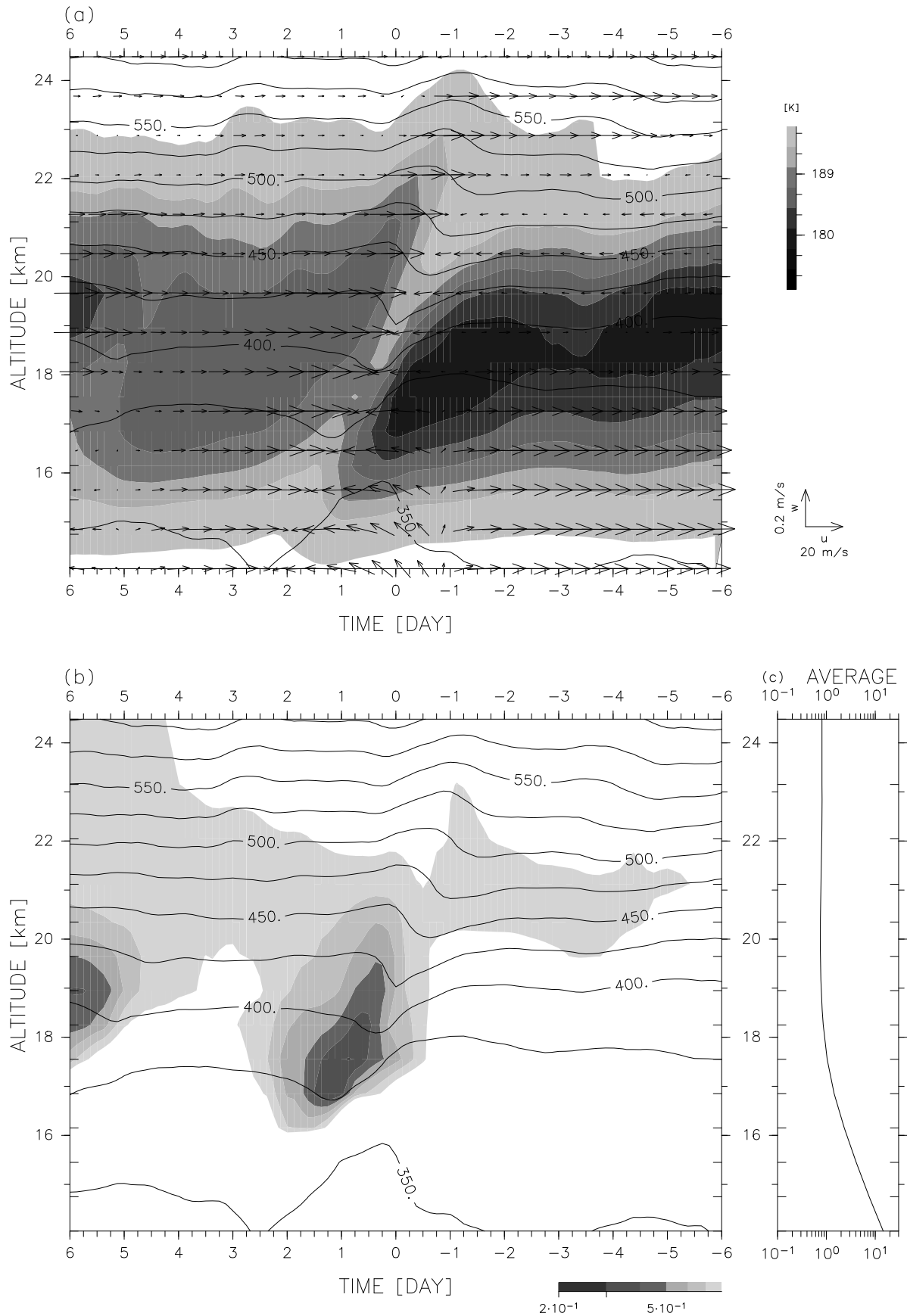


Figure 17

lapse-rate tropopause was slightly lower than that from observations [Dessler *et al.*, 2006]. For 3.5 km grid (7 km grid) data, the average frequency of lapse-rate tropopause penetration for 5°S–5°N is 0.17% (0.25%). We also found that estimating the overshooting probability based on the boundary layer equivalent potential temperature and the tropopause potential temperature might not reflect reality.

[41] We investigated major disturbances that control temperature and water vapor in the TTL. The temperature and water vapor mixing ratio around the tropopause at a zonal scale of ~12,000 km are controlled mainly by equatorial Kelvin waves generated by a super cloud cluster (SCC-A). Very cold points are found on the cold phase of Kelvin waves, resulting from gravity waves with a horizontal scale of ~600 km and superimposed on a cold phase. The gravity waves are generated by a second super cloud cluster (SCC-B) located to the east of SCC-A, which generated large-amplitude Kelvin waves in the TTL. The meeting of the cold phases of these two waves resulted in very cold temperatures in the TTL. If such a positional relationship is a common feature of organized convection, this mechanism could be an important dehydration process in the TTL. It should be emphasized that cloud organization and wave generation may be more important in the TTL than are individual cumulus cloud processes.

[42] The model also simulated a gigantic cumulus cloud system: a super convective system (SCS) with a zonal scale of 1100 km. We investigated the in-cloud properties of the SCS. The highest cloud top is located at 19.6 km; the clouds overshoot the tropopause by ~1 km. Tropopause height and temperature in the region of deep convective clouds are generally lower than those of the environment. We also found two local minima in the temperature profile around the tropopause. The lower minimum is directly influenced by the deep convection, while the upper minimum is caused by gravity waves generated by the SCS. The gravity waves caused downward motions above the SCS and may have played a role in preventing the cloud top from penetrating deep into the lower stratosphere. It is suggested that a detailed consideration of cloud and wave dynamics is necessary to understand the overshooting process.

[43] It was not possible to perform an analysis of water vapor budget in the TTL because of inadequate (excessively dry) initial stratospheric conditions and an excessively short integration time. High variability in water vapor within the TTL was caused by Kelvin waves, associated not with condensation drying in the cold phases but with dry air transport from the tropical lower stratosphere in the warm phases. Previous observations have revealed that dry air transport by Kelvin waves is an important process in terms of water vapor control.

[44] Our results demonstrate that interaction between small- and large-scale processes is essential in the TTL in terms of dehydration and transport within the TTL. In particular, cloud organization and wave generation are the keys to understanding water vapor control in the TTL. The global, nonhydrostatic model NICAM is an appropriate tool with which to investigate such interactions.

[45] **Acknowledgments.** We would like to thank Hirofumi Tomita and other researchers responsible for the development of NICAM. Com-

ments on the manuscript by three anonymous reviewers are greatly appreciated. Figures 1–17 were produced using the GFD-DENNOU Library. This study was supported in part by the CASIO Science Promotion Foundation, the Circle for the Promotion of Science and Engineering, and the Cooperative Research Program of the Center for Climate System Research, University of Tokyo. The NICAM experiments were performed using the Earth Simulator housed at JAMSTEC.

## References

- Andrews, D. G., J. R. Holton, and C. B. Leovy (1987), *Middle Atmosphere Dynamics*, 489 pp., Academic Press, San Diego, Calif.
- Brewer, A. W. (1949), Evidence for a world circulation provided by the measurements of helium and water vapor distribution in the stratosphere, *Q. J. R. Meteorol. Soc.*, *75*, 351–363.
- Chaboureaud, J.-P., J.-P. Cammas, J. Duron, P. J. Maseart, N. M. Sitnikov, and H.-J. Voessing (2007), A numerical study of tropical cross-tropopause transport by convective overshoots, *Atmos. Chem. Phys.*, *7*, 1731–1740.
- Chen, S. S., R. A. House Jr., and B. E. Mapes (1996), Multiscale variability of deep convection in relation to large-scale circulation in TOGA COARE, *J. Atmos. Sci.*, *53*, 1380–1409.
- Ciesielski, P. E., R. H. Johnson, P. T. Haertel, and J. Wang (2003), Corrected TOGA COARE sounding humidity data: Impact on diagnosed properties of convection and climate over the warm pool, *J. Clim.*, *16*, 2370–2384.
- Corti, T., et al. (2008), Unprecedented evidence for deep convection hydrating the tropical stratosphere, *Geophys. Res. Lett.*, *35*, L10810, doi:10.1029/2008GL033641.
- Danielsen, E. F. (1982), A dehydration mechanism for the stratosphere, *Geophys. Res. Lett.*, *9*(6), 605–608.
- Danielsen, E. F. (1993), In situ evidence of rapid, vertical, irreversible transport of lower tropospheric air into the lower tropical stratosphere by convective cloud turrets and by large-scale upwelling in tropical cyclones, *J. Geophys. Res.*, *98*(D5), 8665–8681.
- Dessler, A. E., S. P. Palm, and J. D. Spinhilne (2006), Tropical cloud-top height distributions revealed by the Ice, Cloud, and Land Elevation Satellite (ICESat)/Geoscience Laser Altimeter System (GLAS), *J. Geophys. Res.*, *111*, D12215, doi:10.1029/2005JD006705.
- Folkins, I. (2002), Origin of lapse rate changes in the upper tropical troposphere, *J. Atmos. Sci.*, *59*, 992–1005.
- Folkins, I., M. Loewenstein, J. Podolske, S. J. Oltmans, and M. Proffitt (1999), A barrier to vertical mixing at 14 km in the tropics: Evidence from ozonesondes and aircraft measurements, *J. Geophys. Res.*, *104*(D18), 22,095–22,102.
- Folkins, I., S. J. Oltmans, and A. M. Thompson (2000), Tropical convective outflow and near surface equivalent potential temperatures, *Geophys. Res. Lett.*, *27*(16), 2549–2552.
- Folkins, I., P. Bernath, C. Boone, G. Lesins, N. Livesey, A. M. Thompson, K. Walker, and J. C. Witte (2006), Seasonal cycles of O<sub>3</sub>, CO, and convective outflow at the tropical tropopause, *Geophys. Res. Lett.*, *33*, L16802, doi:10.1029/2006GL026602.
- Fueglistaler, S., M. Bonazzola, P. H. Haynes, and T. Peter (2005), Stratospheric water vapor predicted from the Lagrangian temperature history of air entering the stratosphere in the tropics, *J. Geophys. Res.*, *110*, D08107, doi:10.1029/2004JD005516.
- Fueglistaler, S., A. E. Dessler, T. J. Dunkerton, I. Folkins, Q. Fu, and P. W. Mote (2009), Tropical tropopause layer, *Rev. Geophys.*, *47*, RG1004, doi:10.1029/2008RG000267.
- Fujiwara, M., and M. Takahashi (2001), Role of the equatorial Kelvin wave in stratosphere-troposphere exchange in a general circulation model, *J. Geophys. Res.*, *106*(D19), 22,763–22,780.
- Fujiwara, M., K. Kita, and T. Ogawa (1998), Stratosphere-troposphere exchange of ozone associated with the equatorial Kelvin waves as observed with ozonesondes and rawinsondes, *J. Geophys. Res.*, *103*(D15), 19,173–19,182.
- Fujiwara, M., F. Hasebe, M. Shiotani, N. Nishi, H. Vömel, and S. J. Oltmans (2001), Water vapor control at the tropopause by equatorial Kelvin waves observed over the Galápagos, *Geophys. Res. Lett.*, *28*(16), 3143–3146.
- Fujiwara, M., et al. (2009), Cirrus observations in the tropical tropopause layer over the western Pacific, *J. Geophys. Res.*, *114*, D09304, doi:10.1029/2008JD011040.
- Gettelman, A., and T. Birner (2007), Insights into tropical tropopause layer processes using global models, *J. Geophys. Res.*, *112*, D23104, doi:10.1029/2007JD008945.
- Gettelman, A., M. L. Salby, and F. Sassi (2002), Distribution and influence of convection in the tropical tropopause region, *J. Geophys. Res.*, *107*(D10), 4080, doi:10.1029/2001JD001048.

- Grabowski, W. W. (1998), Toward cloud resolving modeling of large-scale tropical circulations: A simple cloud microphysics parameterization, *J. Atmos. Sci.*, *55*, 3283–3298.
- Highwood, E. J., and B. J. Hoskins (1998), The tropical tropopause, *Q. J. R. Meteorol. Soc.*, *124*, 1579–1604.
- Holton, J. R., and A. Gettelman (2001), Horizontal transport and the dehydration of the stratosphere, *Geophys. Res. Lett.*, *28*(14), 2799–2802.
- Holton, J. R., P. H. Hynes, M. E. McIntyre, A. R. Douglass, R. B. Rood, and L. Pfister (1995), Stratosphere-troposphere exchange, *Rev. Geophys.*, *33*, 403–439.
- Johnson, R. H., T. M. Rickenbach, S. A. Rutledge, P. E. Ciesielski, and W. H. Schubert (1999), Trimodal characteristics of tropical convection, *J. Clim.*, *12*, 2397–2418.
- Johnston, H. S., and S. Solomon (1979), Thunderstorms as possible micro-meteorological sink for stratospheric water, *J. Geophys. Res.*, *84*(C6), 3155–3158.
- Kuang, Z., and C. S. Bretherton (2004), Convective influence on the heat balance of the tropical tropopause layer: A cloud-resolving model study, *J. Atmos. Sci.*, *61*, 2919–2927.
- Küpper, C., J. Thuburn, G. C. Craig, and T. Birner (2004), Mass and water transport into the tropical stratosphere: A cloud-resolving simulation, *J. Geophys. Res.*, *109*, D10111, doi:10.1029/2004JD004541.
- Liu, C., and E. J. Zipser (2005), Global distribution of convection penetrating the tropical tropopause, *J. Geophys. Res.*, *110*, D23104, doi:10.1029/2005JD006063.
- Louis, J. (1979), A parametric model of vertical eddy fluxes in the atmosphere, *Boundary Layer Meteorol.*, *17*, 187–202.
- Madden, R. A., and P. R. Julian (1994), Observations of the 40–50-day tropical oscillation—A review, *Mon. Weather. Rev.*, *122*, 814–837.
- Mellor, G. L., and T. Yamada (1974), A hierarchy of turbulence closure models for planetary boundary layers, *J. Atmos. Sci.*, *31*, 1791–1806.
- Nakajima, T., M. Tsukamoto, Y. Tsushima, A. Numaguti, and T. Kimura (2000), Modeling of the radiative process in an atmospheric general circulation model, *Appl. Opt.*, *39*, 4869–4878.
- Nakazawa, T. (1988), Tropical super clusters within intraseasonal variations over the western Pacific, *J. Meteorol. Soc. Jpn.*, *66*, 823–839.
- Nasuno, T. (2008), Equatorial mean zonal wind in a global nonhydrostatic aquaplanet experiment, *J. Meteorol. Soc. Jpn.*, *86A*, 219–236.
- Nasuno, T., H. Tomita, S. Iga, H. Miura, and M. Satoh (2007), Multiscale organization of convection simulated with explicit cloud processes on an aquaplanet, *J. Atmos. Sci.*, *64*, 1902–1921.
- Nasuno, T., H. Tomita, S. Iga, H. Miura, and M. Satoh (2008), Convectively coupled equatorial waves simulated on an aquaplanet in a global nonhydrostatic experiment, *J. Atmos. Sci.*, *65*, 1246–1265.
- Neale, R. B., and B. J. Hoskins (2000), A standard test for AGCMs including their physical parameterizations: I. The proposal, *Atmos. Sci. Lett.*, *1*, 108–114, doi:10.1006/asle.2000.0019.
- Newell, R. E., and S. Gould-Stewart (1981), A stratospheric fountain?, *J. Atmos. Sci.*, *38*, 2789–2796.
- Numaguti, A., M. Takahashi, T. Nakajima, and A. Sumi (1997), Description of CCSR/NIES atmospheric general circulation model, *CGER's Supercomput. Monogr. Rep.* 3, pp. 1–48, Natl. Inst. for Environ. Stud., Ibaraki, Japan.
- Parker, D. E. (1973), Equatorial Kelvin waves at 100 millibars, *Q. J. R. Meteorol. Soc.*, *99*, 116–129.
- Pfister, L., K. R. Chan, T. P. Bui, S. Bowen, M. Legc, B. Gary, K. Kelly, M. Proffitt, and W. Starr (1993), Gravity waves generated by a tropical cyclone during the STEP tropical field program: A case study, *J. Geophys. Res.*, *98*(D5), 8611–8638.
- Potter, B. E., and J. R. Holton (1995), The role of monsoon convection in the dehydration of the lower tropical stratosphere, *J. Atmos. Sci.*, *52*, 1034–1050.
- Satoh, M., T. Matsuno, H. Tomita, H. Miura, T. Nasuno, and S. Iga (2008), Nonhydrostatic Icosahedral Atmospheric Model (NICAM) for global cloud resolving simulations, *J. Comput. Phys.*, *227*, 3486–3514.
- Seidel, D. J., R. J. Ross, and J. K. Angell (2001), Climatological characteristics of the tropical tropopause as revealed by radiosondes, *J. Geophys. Res.*, *106*(D8), 7857–7878.
- Sherwood, S. C., and A. E. Dessler (2000), On the control of stratospheric humidity, *Geophys. Res. Lett.*, *27*(16), 2513–2516.
- Sherwood, S. C., and A. E. Dessler (2001), A model for transport across the tropical tropopause, *J. Atmos. Sci.*, *58*, 765–779.
- Sherwood, S. C., J.-H. Chae, P. Minnis, and M. McGill (2004), Underestimation of deep convective cloud tops by thermal imagery, *Geophys. Res. Lett.*, *31*, L11102, doi:10.1029/2004GL019699.
- Tomita, H., and M. Satoh (2004), A new dynamical framework of nonhydrostatic global model using the icosahedral grid, *Fluid Dyn. Res.*, *34*, 357–400.
- Tomita, H., H. Miura, S. Iga, T. Nasuno, and M. Satoh (2005), A global cloud-resolving simulation: Preliminary results from an aqua planet experiment, *Geophys. Res. Lett.*, *32*, L08805, doi:10.1029/2005GL022459.
- Tsuda, T., Y. Murayama, H. Wiryosumarto, S. Woro, B. Harijono, and S. Kato (1994), Radiosonde observations of equatorial atmosphere dynamics over Indonesia I. Equatorial waves and diurnal tides, *J. Geophys. Res.*, *99*(D5), 10,491–10,505.
- Wheeler, M., G. N. Kiladis, and P. J. Webster (2000), Large-scale dynamical fields associated with convectively coupled equatorial waves, *J. Atmos. Sci.*, *57*, 613–640.

M. Fujiwara and H. Kubokawa, Graduate School of Environmental Science, Hokkaido University, N10, W5, Sapporo 060-0810, Japan. (uma@ees.hokudai.ac.jp)

T. Nasuno, Research Institute for Global Change, Japan Agency for Marine-Earth Science and Technology, 3173-25 Showamachi, Kanazawa-ku, Yokohama, Kanagawa 236-0001, Japan.

M. Satoh, Center for Climate System Research, University of Tokyo, 5-1-5, Kashiwanoha, Kashiwa, Chiba 277-8568, Japan.